

Strain Hardening in Aerospace Alloys

R. K. Gupta^{1*}, Christy Mathew², P. Ramkumar¹

¹Materials and Mechanical Entity, Vikram Sarabhai Space Centre, Trivandrum-22

²Mar Athanasius College of Engineering, Kothamangalam-686666

*rohitkumar_gupta@vssc.gov.in

Abstract

Strain hardening is one of the important strengthening mechanisms, which plays significant role in processing and application of metals and alloys. For non-heat treatable alloys, it becomes more important. Its effect is different in different metals and alloys and accordingly specific process and application regime are selected. A large variety of metals and alloys from the family of light alloys (Al, Ti based), high strength steels and high temperature alloys (Co, Ni and Nb based) are used in aerospace systems. This paper analyses importance of strain hardening phenomenon in these alloys. Attempts are made to explain the differential behaviour of various alloys in governing the tensile to yield strength ratio along with % elongation. Role of temperature in this behaviour is also included.

Keywords

Strain Hardening; Aerospace Alloys; Ti6Al4V; Maraging Steel; Al Alloys

Introduction

Strain hardening or work hardening is one of the most commonly used means of improving strength of an alloy. In a simple way it is the use of permanent deformation to increase the strength of the metal. It is either denoted by tempers (as half hard, full hard, spring temper, etc.) in case of steels or by % cold work in case of light metals/alloys (aluminium/ titanium). Strain hardening in metals, i.e. the capacity of the material where flow stress increases with increasing plastic strain, is being studied since the discovery of dislocations, and is still a matter of current interest. Understanding the strain-hardening capability of structural alloys is of practical importance also since it controls their fracture properties and deformability.

Strain hardening is an important industrial process that is used to harden metals or alloys that do not respond to heat treatment. For alloys strengthened by solid-solution addition, rate of strain hardening may be either increased or decreased as compared to pure metals. Dieter explained that the final strength of a cold worked solid solution alloy is mostly greater than that of pure metal cold worked to the same extent at the same temperature. Increasing temperatures reduces strain hardening and accordingly strength. The rate of strain hardening can be assessed from the slope of the true stress-true strain graph (flow curve). Generally, the rate of strain hardening is lower for hcp metals than for cubic metals.

Increase in strength can be seen from schematic Fig. 1 explaining strain hardening phenomenon. It also explains that material shows increase in strength in unloading and reloading. The degree of cold working determines the strength of a metal. As the amount of cold work increases, so does the strength. However, the total elongation also changes with amount of cold work. Harder tempers like spring and super spring have high strength and low ductility (bad formability), whereas softer tempers like annealed and 1/4 hard have low strength and high ductility (very good formability). When choosing a material for specific application, it is best to use the highest strength material that still meets the formability requirements of the design.

As the percentage cold work increases, there is a diminishing increase (increase with lower rate) on strength. Generally it is seen that increase in strength with increase in cold work results in lowering of % elongation. This is due to the fact that at higher amount of reductions, there are fewer free dislocations to become entangled. Since the material is less able to plastically deform, fracture becomes much more likely. At high levels of cold work, the material becomes very difficult to further process or form. If it must be formed, or reduced further in thickness, then annealing becomes necessary. Extent of reduction/ changes in ductility due to cold work is different for

different alloys. It depends on several other factors like type of alloy, stacking fault energy, number of phases, strain hardening behaviour and strengthening mechanisms in the alloy.

Strain hardening results from the interaction of dislocations with each other and with the various constituents of the microstructure, such as, grain boundaries, precipitates and solutes, etc. When a material is permanently deformed, the dislocations move until they are stopped in the crystalline lattice. The most effective dislocation barriers are another dislocation. Where dislocations run on different planes and intersect, they cannot pass through each other. Finally, dislocations pile up against each other, and become inter-twined. This dislocation entanglement prevents further permanent deformation of that particular grain, without use of significantly greater energy. This greatly increases the strength of the material in subsequent loading.

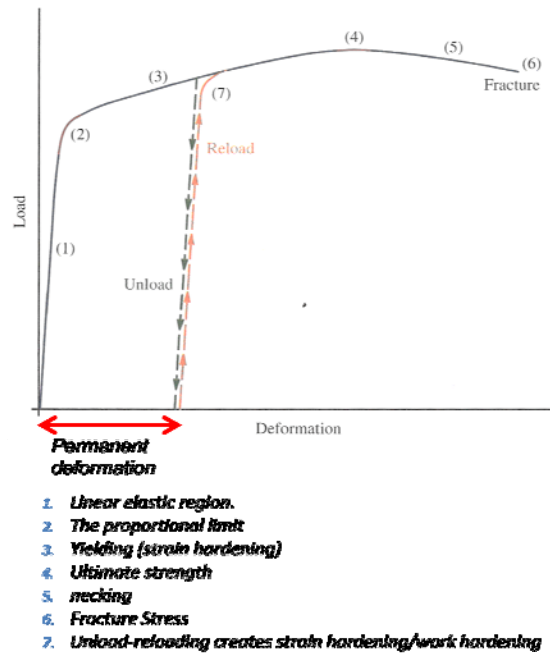


FIG. 1: SCHEMATIC REPRESENTATION OF STRAIN HARDENING

Varieties of alloys in various forms are used in aerospace systems, which are realised through different processing techniques. Strain hardening has important role in processing as well as in application of these materials. This phenomenon has been extensively studied and reported. However, its role and importance in aerospace alloys has not been discussed adequately. The present paper attempts to highlight, analyse and review this important phenomenon in aerospace alloys.

Effect of Strain Hardening

Strain Hardening and Plastic Instability

Plastic instability is another condition, which is closely associated with strain hardening phenomenon. It is an established fact that necking is the result of a trade-off (during deformation) between the strain hardening process within the material and the level of the applied stress. Metals generally show a reduced strain hardening with increasing strain while the level of the stress continues to increase. At some point, the two values cross and the material is plastically unstable and the smallest of defects is sufficient to promote localized deformation at that position. Essentially all deformation is localized thereafter in the necked region until fracture occurs. The greater the strain hardening coefficient, the plastic instability is delayed. Delaying plastic instability to higher strain levels is desirable for forming operations and also for increased toughness. Plastic instabilities continue to be a real concern in the design of structures. Strain localization is mostly promoted by large inclusions, by triaxial stresses (e.g. sharp notches and cracks) and are pronounced in materials with low strain hardening and low strain rate hardening.

Kujawski and Ellyin showed that for a strain hardening material, the plastic zone size in plane stress is affected as a result of strain hardening. The larger the strain hardening, the greater the strain to instability. It would thus appear that the ductility is increased by decreasing the volume fraction and size of particles (fewer voids nucleated) and that it is especially effective in materials of high strain hardening.

Strain Hardening and Fracture

Griffith explained the fracture problem arising from small cracks and computed the fracture stress, while Orowan applied this result to materials which had some degree of plasticity by adding an additional term to the true surface energy with the plastic deformation. Thus more realistic picture that develops for most structural materials is that some plasticity occurs at the crack tip and with continued loading, the size of the plastic zone at the crack tip increases, eventually leading to fracture. Of course while the size of the zone increases, the strain at the crack tip increases as well. Eventually a critical strain is reached and fracture takes place.

The plastic strain has a significant effect on the energy that may be absorbed at the tip of a sharp crack. It means plastic strain (localization) plays a key role in the fracture resistance of metals. Strain localization on a macroscopic scale is delayed in smooth bars by increasing the strain hardening coefficient to promote more uniform deformation. This implies rather directly that all things being equal, the fracture toughness of a material increases with increasing strain hardening. Petch and Armstrong described the strain hardening phenomenon for steel and other reasonably cleavage-prone materials that, on loading a pre-cracked material, the plastic zone at the tip of the crack strain hardens until the cleavage stress is reached and the material fractures.

Most of the strengthening methods of material raise the yield stress without changing the cleavage fracture stress and so the fracture toughness decreases. But strengthening through strain hardening phenomenon increases fracture stress also and correspondingly fracture toughness. For example, grain refinement raises the material yield stress but the fracture stress is raised even more and so the fracture toughness. In case of low strain hardening, very little hardening occurs ahead of crack and deformation is localized to a small strip. However, an alloy having significant strain hardening will have a large plastic zone because once the material directly in front of the crack deforms, it becomes harder than the non-deformed material and deformation spreads in both the lateral and forward directions. All factors being equal, the material with high strain hardening exhibits high fracture toughness.

The work of Hahn and Rosenfield provides a simple example of the factors affecting the fracture toughness:

$$K_{IC} = n\sqrt{cE\sigma_{ys}\epsilon_f}$$

where K_{IC} is the plane strain fracture toughness, n the strain hardening coefficient, σ_{ys} the yield strength, ϵ_f fracture strain, E the Young's modulus, and c is a constant depending on the state of stress.

Strain Hardening in Nano Grained Material

The small grain size of nano materials makes them quite different from the bulk material in a number of ways. For example, at high and moderate strain rates, the nanomaterials exhibit very low ductility at room temperature. However, at very low strain rates (less than 10^{-4} s^{-1}), very large strains are usually observed in fcc nanomaterials. This is due to an extremely high strain rate sensitivity coefficient ' m ' which is analogous to that observed in high-temperature superplasticity of micro-grained materials. Consequently, the deformation mechanism at room temperature and low strain rate resembles that for high-temperature superplasticity. This results in large amount of deformation. It means high strain hardening assists in large deformation at very low strain rates. Indeed, Coble creep (enabling both the grain boundary sliding and grain rotation) can operate according to the Ashby–Verall.

Strain Hardening and Other Properties

Material having good strain hardening behaviour also produces changes in other physical properties through cold working. There is usually a small decrease in density of the order of few tenths of a per cent, decrease in electrical conductivity due to an increased number of scattering centres, and a small increase in the of thermal expansion.

Because of the increased internal energy of the cold worked state, chemical reactivity is increased. This leads to a general decrease in corrosion resistance and in certain alloys introduces the possibility of 'stress corrosion cracking'.

Strain Hardening Parameters and Its General Effects

Strain Hardening Coefficient and Strength

Dieter et al. and Ebrahimi et al. explained that the strain hardening coefficient has major role in the forming operation, which controls the amount of uniform plastic strain in the material before strain localization or necking. A simple power curve relation express the flow curve of many metals in the region of uniform plastic deformation, that is, from yielding to maximum load $\sigma = K\varepsilon^n$, where n is the strain-hardening coefficient, and K is the strength coefficient. Zhang et al. also described that the strain hardening coefficient and strength are the basic mechanical parameters of metallic material performance. Ebrahimi et al. described that maximum amount of uniform plastic deformation in tensile straining is given by the strain-hardening coefficient (n). A standard method to evaluate it is based on stress–strain data obtained from uniaxial tensile test. Stress–strain curves are usually represented by the Holloman equation. Therefore, by plotting stress–strain data on logarithmic coordinates, it can be shown that the slope of the line in the fully plastic region defines the strain-hardening coefficient (n).

Similarly, the intersection between the stress axis of the stress strain curve and the extrapolated line of the true stress strain curve gives the value of the strength. The relationship between K value and temperature and strain rate is similar to the strain hardening coefficient value. It decreases with the temperature and increases as the strain rate increases. Further, mechanical behaviour of superplastic materials is normally described by the power-law relationship between the equivalent stress σ , equivalent strain ε and equivalent strain-rate $\dot{\varepsilon}$ as $\sigma = K\varepsilon^n \dot{\varepsilon}^m$ where n is the hardening index, m the strain-rate sensitivity index and K a material constant.

Strain, Strain Hardening and Strain Hardening Rate

Luo et al. explained that the strain hardening coefficient n is the result of balance between strain hardening mechanism depending mainly on strain, and softening mechanism depending on time. The strain hardening coefficient increases with the increase in strain. The yield strength and the strain hardening increases with the increasing strain rate at a fixed temperature but decreases with increasing temperature for a given strain rate. Role of strain rate and temperature is highly significant in determining strain hardening behaviour and formability of material. Lee et al. have shown that at constant temperature, the flow stress, strain hardening rate and strain rate sensitivity increases with increase in strain rate.

While increases in the strain hardening rate will increase the strain at instability ε_u (true tensile strain at plastic instability), it is not true that increases in σ_i (Friction stress for yielding in Hall–Petch equation) have the same effect. In fact, increasing σ_i without a corresponding increase in the strain hardening rate will lower ε_u , as is known from the Considere criteria.

Grain size of material also has important effect on strain hardening. As the grain size decreases, the yield and flow stresses increase without a corresponding increase in the strain hardening and some decrease in ductility is observed. The effects even for a given material are not always obvious. For example, Morrison and Miller showed that for titanium and Fe–Ni alloy, there was a decrease in uniform strain with decreasing grain diameter as compared for other steel and titanium materials in which there was an increase in the reduction in area with decreasing grain diameter. These two opposing behaviours can be understood with different degree of H–P dependence.

Dynamic strain ageing (DSA) is another important phenomenon, which initially produces a rapid increase in the strain-hardening rate with straining. However, when the supply of interstitial atoms (for dislocation locking) is no longer sufficient, the strain hardening decreases. Increased interstitial content delays the onset of instability. In high nitrogen steels (0.03%), neither decrease in strain hardening rate nor any reduction in ductility was noted.

In fcc material, when σ_i is lower, favouring higher values of the instability strain, ϵ_u . There is no major effect of reducing the temperature or increasing the strain rate on σ_i . However, both of these factors lead to increased dislocation storage and increased strain hardening, thus leading to increasing the strain at instability. Composition changes can also be very important. As an example, the case of 70–30 brass is instructive. In this material, alloying tends to increase the strength. However, the SFE is also lowered delaying the onset of cross slip which maintains a relatively high strain hardening rate. Thus compared to Cu, where the strain hardening decreases with increasing strain, ϵ_u is greater.

In hcp materials like Mg, Zn, Cd and Be, the primary slip system, basal, is similar to fcc. However, there are only two independent slip systems on this plane. Thus other non-close packed systems such as prism and pyramidal as well as possible twinning must be activated for generalized polycrystalline deformation. The stress for basal slip is not strongly temperature dependent. However, the stresses for the secondary systems are strongly temperature dependent. The effect of these behaviours on the polycrystalline yield stress is that σ_i shows little change with temperature. However, the microstructural stress intensity parameter is related to slip accommodation between neighboring grains and thus it becomes temperature dependence and yield increases with decreasing temperature favouring a reduction in ϵ_u at lower temperatures. Opposing this trend is the fact that the strain hardening becomes higher at lower temperatures. The net effect of these two factors is that ϵ_u increases at lower temperatures. For slip in Zr and α -Ti, the primary slip system is prismatic. In these metals, σ_i is very much higher than for those metals whose primary deformation mode is basal slip. The PN stress again dominates and there is a large increase in σ_i at low temperatures. The net effect is that ϵ_u is low and decreases even more at low temperatures. ϵ_u can be understood in terms of the two competing terms in the Hall–Petch equation and details of the deformation process.

Strain Hardening in Aerospace Alloys

Ti and Ti Alloys

1) Commercially Pure Ti

At room temperature CP-Ti has moderate formability and limited ductility. Although it has hcp structure only a few slip systems are active. Therefore twin systems are necessary in order to obtain good amount of deformation. However, twinning is also limited at {1012} and {1011}. Accordingly deformation is carried out at elevated temperatures where basal slip systems can be activated. Chun and Wen-feng conducted a hot compression experiment on commercially pure Titanium under high temperatures ranging from 700 to 900°C with 50°C interval and at a strain rate 3.6 to 40 per minute. It was noted that dynamic recrystallization occurs at 900°C, dynamic recovery takes place at temperature range from 750 to 850°C, and the strain hardening phenomenon occurs at lower temperature of 700 °C.

Furhter, Tsao et al. conducted a study on its flow stress behaviour during warm tensile deformation of sheet specimen. It shows (Table 1) that the strain hardening coefficient of the CP-Ti sheet increases with the increase in strain rate and decrease in deformation temperature.

TABLE 1: STRAIN HARDENING COEFFICIENT OF CP-TI AT VARIOUS TEMPERATURES AND STRAIN RATE

Temperature (°C)	<i>n</i> value at different Strain rates (per sec)			
	5×10^{-2}	1.6×10^{-2}	2.5×10^{-3}	8.3×10^{-4}
350	0.27114	0.23338	0.21536	0.1897
400	0.25602	0.21521	0.19058	0.16218
450	0.22366	0.19813	0.16278	0.13668
500	0.21171	0.15973	0.13912	0.11974

Ayman et al. conducted a simple compression test, plane strain compression test and simple shear test. In simple shear, the strain hardening rate is much lower than in other two simple tests. In simple compression and in plane strain compression, the strain hardening behavior is found to be in three stages. First stage consists of a dynamic recovery regime and the second stage a region with increasing strain hardening rate. The third stage is

characterized by a falling strain hardening rate. The increase in the strain hardening rate in first stage is due to deformation twinning and not due to dynamic strain aging. The falling strain hardening rate in third stage can be expected to be a result of increasing the difficulty of producing deformation twin.

Also, Purceka et al. explained that CP Ti could be uniformly processed through equal channel angular extrusion (ECAE) upto 8 passes. Significant improvement in the strength levels with adequate ductility is because of the grain refinement and the strain hardening without alloying.

2) *Ti Alloy Ti6Al4V*

Luo et al. explained the flow stress–strain curves of Ti–6Al–4V alloy in $\alpha + \beta$ two-phase region and β single-phase region at different strain rates and deformation temperatures. In both cases, isothermal compression behaviour exhibits a peak flow stress at a very low strain followed by extensive flow softening where softening rate is higher at low strains and considerably less at higher strains. This phenomenon is related to the fact that the dominant deformation mechanism is due to slip of dislocations at low strains. Thus, the dislocation density increases quickly with increasing plastic strain. Then, the softening effect plays an important role in dislocation density evolution and with further increase of strain, flow stress sharply decreases to a steady value when the dynamic softening effect is sufficient to counteract the strain hardening effect. The strain hardening coefficient 'n' results from a balance between hardening mechanisms depending mainly on strain and softening mechanisms depending mainly on time. The strain affects significantly the strain hardening coefficient 'n' due to the change in grain size of primary phase, and the competition between thermal softening and strain hardening.

It is reported that the strain hardening coefficient is not constant but it changes as the strain rate changes. It decreases as the strain rate decreases due to decrease in the dislocation density.

Lee et al. conducted a study on the impact behaviour of Ti-6Al-4V alloy at -150 °C, 0 °C and 25 °C and at different strain rates. The strain hardening coefficient value for the low temperature testing was found to be larger as given in the Table 2. In this study, it has been also confirmed that the flow stress depends on both the strain and the strain rate. Specifically, for a constant strain, the flow stress increases rapidly with increasing strain rate, while for a constant strain rate, the flow stress increases gradually with increasing strain. Also it explains that the strain hardening coefficient (n) increases with increasing strain rate at a fixed temperature, but decreases with increasing temperature for a given strain rate. This result suggests that a lower deformation temperature increases the density and multiplication rate of the dislocations within the Ti–6Al–4V microstructure, and prompts a corresponding improvement in the resistance of the alloy to plastic flow.

TABLE 2: STRAIN HARDENING COEFFICIENT VALUES AT VARIOUS TEMPERATURES AND STRAIN RATE

Temperature (°C)	Strain rate (s ⁻¹)	Strain hardening coefficient
-150	4300	0.4021
	3000	0.3749
	1000	0.3414
0	4300	0.3361
	3000	0.3183
	1000	0.2967
25	4300	0.3266
	3000	0.3091
	1000	0.2877

Lee showed that for specimens deformed at different temperatures after the yielding, the flow curve firstly is of parabolic shape until the true strain accumulates to about 0.075, and then becomes linear under a specific strain hardening rate. It is also seen that the increase of temperatures has a very pronounced effect on the magnitude of the flow stress, i.e. the flow stress decreases dramatically with an increase in temperature, which indicates that a rapid softening occurs in the high temperature regimes, and that the dislocations annihilate far more rapidly than they generate. From this study it is also found that the mechanical properties of this material are

fairly sensitive to temperature. It is noted that under the present test conditions, the yield strength and the strain hardening rate decrease with increasing temperature. This can be explained by the fact that increasing temperature decreases the density and multiplication rate of dislocations, and consequently, resulting in a loss of resistance to plastic flow, leading to, the material becomes softer and more ductile. When a material deforms under high temperature and high strain-rate conditions, its flow behavior is predominated by a competition process between the rate of strain hardening and the rate of thermal softening.

Generally, high-rate deformation can cause the enhancement of a material's strength due to the high rate of strain hardening. By contrast, an increase of temperature will lead to a rapid reduction in the rate of strain hardening. When thermal softening becomes dominant, the plastic flow is controlled completely by the temperature effect, which results in a rapid drop of flow stress. Therefore, although the plastic deformation proceeds at a high strain rate, not only is the effect of the strain rate, but also the effect of temperature, found on strength: however, the latter has more pronounced effect than the former.

Morita showed STQ-treated (ST+ quenched) material indicating strong strain hardening. When the material at the STQ condition was further aged, the degree of strain hardening decreased as the aging temperature increased. This tendency was reflected in the change in the ratio of YS/ TS, namely, this ratio was lowest at the STQ condition and recovered with increasing aging temperature.

Steels

1) Carbon Steel and HSLA Steel

Strain hardening behaviour of Ti, micro-alloyed steels and ferritic-pearlitic steels depends significantly on the microstructure. There is a very significant relationship between the microstructure of steels and their strain hardening behaviour. Small precipitates or increasing volume fraction of hard second phase increase the strain hardening rate. Strain hardening rate increases with decreasing particle size of hard Ti(C, N) precipitates or increasing volume fraction of pearlite in ferrite.

Influence of pearlite morphology on strain hardening behaviour is rather small. b.c.c, steels have a smaller strain hardening rate than f.c.c, steels. The microstructure dependence of the strain hardening rate depends on the stability of the steels. The temperature influence on the strain hardening rate is larger in f.c.c, steels than in ferritic b.c.c. steels for both small and large deformations.

Steel characterized by high strain hardening at room temperature and having low strain-hardening capability behave differently under cold forming. It shows smoother surface finish for the former and barreling/ bulging for latter indicating clear phenomenon of uniform elongation by strain hardening.

2) Austenitic Stainless Steel (300 Series)

Austenitic stainless steel is thermodynamically stable over a wide range of temperatures and it can be hardened only by cold working. T.S. Byun et al. conducted a study on the plastic behaviour and the strain hardening dependence on temperature. The tensile test was done on annealed 304, 316, 316LN and 20 % cold worked 316LN. The steels considered for the study showed strong temperature dependence on the strength and ductility. The strength increases as the test temperature decreases. The cold worked specimen tested at room temperature showed high uniform elongation of 40% to 100% and relatively small necking elongations. In the annealed and cold worked conditions the strength of stainless steel is found to be decreasing with increasing temperature while the ductility shows peak at room temperature.

Above room temperature the true strain hardening rate decreases monotonically with strain in the uniform deformation region. At room temperature or below steel shows a two stage hardening behaviour. It is reported to decrease with strain below 3-20% and then it experiences an additional increase-decrease cycle before plastic instability. This characteristics of two stage hardening is due to stress induced transformation of austenite to martensite.

Park et al. conducted a study on the strain rate effects on the mechanical behaviour of AISI 300 series of

austenitic steels. In this study it has been explained that at low temperatures (below room temperature) the stainless steel shows two stage sigmoidal deformation which is non-linear hardening behaviour that is dependent on temperature. It is found to have strong dependency between the two stage strain hardening and the temperature.

3) Maraging Steel

Maraging steels in general have a low strain-hardening ability. The engineering stress-strain curve of the maraging steel has a peak stress at relatively small plastic strains followed by continued decrease of stress, leading to a low tensile to yield-strength ratio. However, the observed total elongation is found to be moderate (~10%). A low tensile to yield strength ratio indicates that the tolerance to plastic overload is small as the strain hardening after yield is minimal. Such a characteristic may become a problem in a safe design against sudden overload. However, there is a possibility by which strain hardening of maraging steel (in solutionised condition) can be increased i.e. through transformation induced plasticity (TRIP), which results in higher tensile to yield strength ratio. This phenomenon occurs when it has presence of retained austenite. But, in aged condition resultant improvement in strength due to strain hardening is minimised since primary mechanism of strengthening is through precipitation of intermetallic in martensitic matrix while such precipitation is restricted in presence of austenite. Although, retained austenite transforms to martensite during straining, it is not as strong as maraged martensite. In such condition no significant strain hardening is observed in maraging steel.

Ultrahigh strength steels, maraging M250 and D6AC have been tested at room temperature to determine both monotonic and cyclic stress-strain curves. For the tempered or aged condition, steels had strain hardening coefficients less than 0.10 and showed cyclic softening.

Aluminium Alloys

Strain hardening behaviour of aerospace Al alloys, like AA6061, AA2024, AA7010, AA2014, AA7075 and commercial purity aluminium has been reported. Tensile test samples are tested at a strain rate of 10^{-3} s^{-1} at room temperature. The strain hardening coefficient values are given in Table 3. It is clear from Table 3 that Al alloys have very low strain hardening among aerospace alloys. However, formability of alloy is found to be good where SFE plays important role in deformation of alloy along with fcc crystal structure.

TABLE 3: STRAIN HARDENING COEFFICIENT OF VARIOUS AL ALLOYS

SL. no.	Alloy	Strain hardening coefficient
1	AA6061	0.23
2	AA2024	0.16
3	AA7075	0.21
4	AA7010	0.07
5	AA2014	0.12
6	CP Al	0.17

High Temperature Materials

Among the materials used for high temperature applications, Ni based superalloy Inconel 718, Co based superalloy Hayens-25 and refractory alloy C-103 are the important materials for space application. Zhang et al. studied and explained that strain hardening and flow softening occurs when Inconel 718 is superplastically deformed. It is well known that grain growth plays an important role in the hardening of superplastic materials where, dynamic recovery, cavitation formation, grain refinement and dynamic precipitation contribute to flow softening. This is a tradeoff between hardening and softening. Strain hardening and superplastic phenomenon are closely related and strain hardening helps to get high elongation under slow strain rate tension.

Lee fitted stress-strain relations using the simple model proposed by Ludwik. The results show that the yield strength and strain hardening coefficient increase with increasing strain rate at a constant temperature (n varies

between 0.28-0.44), but decrease with increasing temperature at a constant strain rate. This suggests that a lower deformation temperature increases the density and multiplication rate of the dislocations within the Inconel 718 microstructure, and prompts a corresponding increase in the plastic flow resistance.

Due to low stacking fault energy of Co, resulting in interaction between stacking faults, high strain hardening rates are reported (strain hardening coefficient of L-605: 0.83). It results in high degree of resistant to necking. Cross slip is difficult in these alloys. However, C-103 alloy has low rate of strain hardening. It has 1% Ti, which improves the ductility of alloy. Although rate of strain hardening is low, Nb being bcc structure, having large number of slip system, some of which get active in the alloy and results in good ductility.

Discussion

The aerospace sector has traditionally been a promoter for the development and application of advanced engineering materials, where component performance is primarily determined by mechanical properties such as strength, stiffness, and damage tolerance as well as by physical and chemical properties such as density, corrosion resistance at ambient and high temperatures. However, behaviour of alloys is primarily governed by their crystal structure and deformation mechanisms. Considering these facts, structural materials for aerospace systems are selected on the basis of general requirements of high specific strength alongwith functional requirements of specific systems and processing feasibility. A list of important structural alloys with their properties (Table 4) and characteristic stress strain curve (Fig. 2) are presented here.

Though strengthening is primarily contributed by precipitation hardening in several aerospace alloys (especially Al alloys), role of strain hardening has significant importance in most of the alloy systems. Even some of these alloys are not designed with the benefit of strain hardening, it has contribution especially in deciding the amount of elongation through uniform plastic deformation prior to necking. It delays the necking by shifting local deformation towards un-necked region (since starting of necked region becomes strain hardened due to dislocation pile-up). In this way deformation proceeds uniformly throughout the length until the stress crosses the threshold level required to break the dislocation pile-up and then necking (local deformation) starts and develops till break. It means that higher the strain hardening, higher shall be the uniform elongation and correspondingly resulting in higher elongation (total). This aspect has important application for all the materials listed in Table 4. Extent of strain hardening is also indicated (indirectly) through the ratio/ difference in ultimate tensile strength and yield strength. Higher the ratio between these, higher shall be the elongation. In such materials role of strain hardening is higher during deformation. This can be seen from Table 4 that elongation of stainless steels and Haynes-25 is higher. It is interesting to note that, these alloys are single phase (non-heat treatable) alloys and strengthened by solid solution hardening and has important scope of strengthening through strain hardening.

Strain hardening behaviour is very useful in fabrication as well as in application. For example, fabrication methods are designed and decided on the basis of material properties and the extent to allowable deformation with or without intermittent heat treatment (annealing). Stainless steels, Nb alloy and Haynes-25 properties (yield strength and % El) clearly indicate that these alloys have relatively higher formability as compared to other alloys.

Examining further it emerges that it has relation to their close packed crystal structure and available deformation mode. Whereas stainless steel being fcc crystal structure (and single phase austenitic structure) can take large amount of deformation, Nb alloy and Haynes-25 also can take large deformation due to single phase structure even though their crystal structure (bcc and hcp respectively) is not as beneficial like stainless steel (with respect to close packing). In C-103 alloy some more slip planes become active and result in good formability. In Haynes- 25 high strain hardening helps in getting large deformations. Metals and alloys with wider stacking faults (low SFE) like stainless steels strain harden more rapidly and twin easily on annealing. But, in case of Al alloys although it has fcc crystal structure (close packed), it shows relatively lower strain hardening behaviour. Primarily it is due to multiple phase alloys where strengthening is mainly by precipitation hardening and role of strain hardening is limited to the extent of allowable forming during tube stretching/ cold rolling/ roll bending. However, here another phenomenon of deformation i.e. cross slip helps in increasing the formability of the alloy in cold deformation and

cryogenic ductility. This is due to very high stacking fault energy. Its benefits are used in plate/ sheet forming/ roll bending to realise large capacity propellant tanks. It means large deformation is possible for a material to either have high strain hardening (n) or have large number of active slip system/ close packed planes or promoted by cross slip.

Observing the properties of high strength steels (maraging steel and Afnor 15CDV6 steel), it can be seen that ratio/ difference in ultimate tensile strength and yield strength is very low and correspondingly it results in lower elongation. Here also strengthening mechanism is through precipitation and fine distribution of second phase. Shifting of deformation due to dislocation pile up/ strain hardening (as in the case of stainless steel) does not take place to large extent. Also crystal structure of these alloys are basically martensitic (bcc/ bct) based where limited slip systems (unlike austenitic stainless steels) are available and cross slip/ twin assisted slip is difficult (unlike Al alloys) due to relatively low stacking fault energy. These alloys are altogether designed for special purpose high strength materials and have other specific benefits, which are used in fabrication and heat treatment. Also design criterion preferred for such alloys are mostly fracture based. Since the strain hardening is low and the UTS to yield ratio/ difference is very low, it is not good for structural design to consider yield stress as limiting criterion. Accordingly structural designer considers fracture toughness as limiting criterion for such materials.

Role of strain hardening in Ti alloys is significant. Though the important alloy Ti6Al4V is a two phase alloy and its cold formability is poor due to spring back property, it has important role during application. The alloy is selected for its specific advantages and primarily used in pressure vessel area where localised deformation is not permitted and cyclic tests are conducted to qualify the component for application at various service conditions. Since it has relatively moderate extent of strain hardening, it is carefully pressurised at a specific safe rate to avoid localised yielding. For example, in a specific instance, pressure vessel was pressurised to a particular level and then depressurised, and in the subsequent pressurization it had shown lower strain as compared to previous pressurization. This is a clear effect of strain hardening. In this alloy, although twinning plays important role in deformation but assistance to slip is limited and hence large deformation in cold condition is limited without intermediate annealing.

TABLE 4: IMPORTANT AEROSPACE ALLOYS AND THEIR TYPICAL MECHANICAL PROPERTIES

Alloys	Condition	Mechanical properties				
		E (GPa)	UTS (MPa)	YS (MPa)	%El	Impact (J)
High strain hardening behaviour alloys						
Stainless steel 304/ 316	Annealed	200	500	210	50	100
Stainless steel 321	Annealed	200	550	210	50	100
Stainless steel 301	Annealed + subzero tested	200	1300	1050	23	60
Stainless steel 202	Annealed	200	700	400	50	200
Co based alloy Haynes-25	Annealed	244	1030	485	50	-
Moderate strain hardening behaviour alloys						
α -Ti alloy ELI Ti5Al2.5Sn	Annealed	110	724	665	10	30
Ti6Al4V	Annealed	110	895	825	12	25
Ti6Al4V	Solution treated +aged	114	1100	1030	10	23
Nb alloy, C-103	Annealed	87	405	310	26	156
Low strain hardening behaviour alloys						
Al alloy AFNOR 7020	Precipitation hardened	71	370	310	12	66
Al alloy AA2014	Precipitation hardened	72.4	470	414	12	60
Al alloy AA2219	Precipitation hardened	73.8	450	350	10	60
M250 Maraging steel	Solution annealing +aging	190	1800	1750	12	95*
AFNOR 15CDV6 steel	Hardened + tempered	210	980	835	13	60

*Fracture Toughness in (MPa \sqrt{m})

It is clear from the above discussion that strain hardening phenomenon has very important role in various stages of

processing/ application of alloy especially for the systems used in aerospace where performance is demanded through alloy selection/ design and reliability is ensured through characterization/ testing.

Considering the above, aerospace structural alloys can be classified under three groups on the basis of strain hardening behaviour. Austenitic stainless steel and Haynes-25 superalloy show highest response to strain hardening, which may be due to single phase fcc structure whereas materials like single phase bcc C-103 alloy and two phase Ti alloys show moderate strain hardening behaviour. Al alloys and high strength steels have lower strain hardening behaviour. Material processing methods are selected accordingly to obtain optimum properties and useful products.

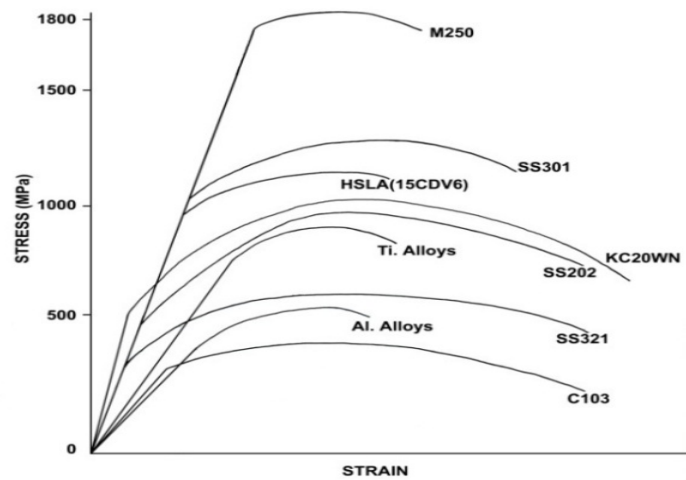


FIG. 2: REPRESENTATIVE STRESS STRAIN CURVE OF VARIOUS AEROSPACE ALLOYS

Summary

Role of strain hardening in aerospace alloys has been reviewed. The strain hardening behaviour of Ti-6Al-4V, CP-Ti, Al alloys, austenitic steels, maraging steels, and high temperature alloys are considered and following points are noted.

1. CP-Ti and Ti-6Al-4V alloy are found to have moderate strain hardening behaviour. The strain hardening coefficient (n) increase with increasing strain rate at a fixed temperature, but decrease with increasing temperature for a given strain rate.
2. Austenitic steels have been identified as materials with high strain hardening. Above room temperature, the true strain hardening rate decreases monotonically with strain in the uniform deformation region. In maraging steel, strain hardening phenomenon is not significant, leading to smaller ratio/ difference in YS to UTS.
3. For Al alloys, strain hardening phenomenon is not significant and coefficient is found to be low.
4. Cobalt based superalloy Haynes-25 has very good response to strain hardening and it provides significant improvement in ductility of the alloy. Nb alloy C-103 has low strain hardening rate but its formability is good due to other mechanisms. Inconel 718 also shows moderate strain hardening behaviour with decreasing trend with increase in temperature.

ACKNOWLEDGEMENT

Authors are thankful to DD, MME, VSSC for necessary guidance and Director VSSC for permission to publish this work.

REFERENCES

- [1] Antolovich S. D., Armstrong R. W., Plastic strain localization in metals: origins and consequences, Progress in Materials Science 59 (2014) 1–160

- [2] Ashby MF, Verrall RA, *Acta Metall* 21 (1973) 149–63.
- [3] ATI Wah Chang Technical data sheet
- [4] Ayman A, Salem 1, Surya R. Kalidindi, Roger D. Doherty, *Acta Mater* 51 (2003) 4225–4237.
- [5] Baird JD, Jamieson A, *J Iron Steel Inst* 204 (1966) 793–803.
- [6] Byun T. S, Hashimoto N., Farrell K., *Acta Mater* 52 (2004) 3889–3899.
- [7] Champion Y, Nowak S, Guerin S, Duhamel C., *Mater Sci Forum*, 567–568 (2007) 29–32.
- [8] Chen FK, Chiu KH, *J Mater Process Technol*, 170 (2005)181–186.
- [9] Cheng L, Poole W, Embury J, Lloyd D. *Metall Mater Trans A*, 34A (2003) 2473–81.
- [10] Chun XU, Wen-feng ZHU, *Trans. nonferrous Met. Soc. China* 20 (2010) 2162 -2167.
- [11] Considere A. Memoire sur l'emploi du fer et de l'acier dans les constructions (On the use of iron and steel in construction) *Ann Ponts Chauss* 9 (1885) 574–775.
- [12] Cottrell AH, Bilby BA, *Proc Phys Soc Lond A*62 (1949) 49–62.
- [13] Dieter G.E., *Mechanical Metallurgy*, McGraw-Hill company (1988) 231-232, ISBN 0-07-100406-8
- [14] Dieter George E., Kuhn Howard A. S. Semiatin Lee, ASM International. *Handbook of Workability and Process Design*. (2003) pp 25.
- [15] Ebrahimi R., Pardis N., Determination of strain-hardening coefficient using double compression test, *Materials Science and Engineering* 518 A (2009) 56–60.
- [16] Eom J.G., Son Y.H., Jeong S.W., Ahn S.T., Jang S.M., Yoon D.J., Joun M.S., *Materials and Design*, <http://dx.doi.org/10.1016/j.matdes.2013.08.101>
- [17] Fang X.F., Dahl W., *Materials Science and Engineering A*203 (1995) 14-25
- [18] Fang X.F., Dahl W., *Materials Science and Engineering A*203 (1995) 36-45
- [19] Fang X.F., Gusek C.O., Dahl W., *Materials Science and Engineering A*203 (1995) 26-35.
- [20] Fribourg G., Bre'chet Y., Deschamps A., Simar A., *Acta Mater* 59 (2011) 3621–3635
- [21] Gil Sevillano J. Flow stress and work hardening. In: Cahn RW, Haasen P, Kramer EJ, editors. *Material science and technology: a comprehensive treatment*, vol. 6 (1993) p. 19–88.
- [22] Giuliano, *Materials and Design* 29 (2008) 1330–1333.
- [23] Griffith AA, *Philos Trans Roy Soc Lond A* 221 (1921) 163–98.
- [24] Hahn GT, Rosenfield AR. Sources of fracture toughness: the relation between K_{Ic} and the ordinary tensile properties of metals. In: *Applications related phenomena in titanium alloys*. ASTM STP, vol. 432. Philadelphia (PA, USA): ASTM International (1968) p. 5–32.
- [25] Hanlon T, Suresh S., Fatigue of nanostructured metals and alloys. In: Carpinteri A, editor. *International conference on fracture (ICF 11)*, Politecnico di Torino, Italy (2005).
- [26] Herchenroeder R.B. and Ebihara W.T., *Metals Engineering Quarterly*, May (1969) 313-323
- [27] Jiao Luo, Li Miaoquan, Yu Weixin, Li Hong, *Materials and Design* 31 (2010) 741–748.
- [28] Jonas J.J., Sellars C.M., McG Tegart W.J., *Metall. Rev.* 130 (1969) 1–24.
- [29] Kashyap K. T., Ramachandra C, Dutta C and Chatterji B, *Bull. Mater. Sci.*, 23, 1 (2000) 47–49.
- [30] Kocks U, Mecking H. *Prog Mater Sci*, 48 (2003) 171–273.
- [31] Kujawski D, Ellyin F. On the size of plastic zone ahead of crack tip. *Eng Fract Mech*, 25 (1986) 229–36.
- [32] Lee Woei-Shyan, Chen Tao-Hsing, Huang Sian-Cing, *Journal of Nuclear Materials* 402 (2010) 1–7.
- [33] Lee Woei-Shyan, Chen Tao-Hsing, Huang Sian-Cing, *Journal of Nuclear Materials* 402 (2010) 1–7.
- [34] Lee Woei-Shyan, Chi-Feng Lin, *Journal of Materials Processing Technology* 75 (1998) 127–136
- [35] Lee Woei-Shyan, Lin Chi-Feng, Chen Tao-Hsing, Hong-Wei Chen, *Materials Science and Engineering A* 528 (2011) 6279–6286

- [36] Mara NA, Bhattacharyya D, Hirth JP, Dickenson T, Misra A. Mechanism of shear banding in nanolayered composites. *Appl Phys Letts* (2010) 97. <http://dx.doi.org/10.1063/1.3458000>.
- [37] Meyers MA, Mishra A, Benson DJ, *Prog Mater Sci*; 51 (2006) 427–556.
- [38] Mithun Kuruvila, Srivatsan T. S., Petraroli M., Park L., *Sadhana*, 33, 3, (2008) 235–250.
- [39] Morrison W.B., Miller R.L. The ductility of ultrafine-grain alloys. In: Burke JJ, Weiss V, editors. *Ultrafine grain metals*. NY: Syracuse University Press (1970) p. 183–211.
- [40] Morrison W.B., *Trans Am Soc Metals* 59 (1966) 824–829.
- [41] Mukhopadhyay C., Rajkumar K., Jayakumar T., Raj B., *J. Mater. Sci.* 45 (2010) 1371–1384.
- [42] Nieh T.G., Wadsworth J., *Mater. Sci. Eng. A* 239–240 (1997) 88–96.
- [43] Nieh T.G., Wadsworth J., Sherby O.D., *Superplasticity in Metals and Ceramics*, Cambridge University Press (1997) p. 137.
- [44] Orowan E., in "Fatigue and Fracture of Metals", Symposium at Massachusetts Institute of Technology, John Wiley & Sons, Inc New York (1952).
- [45] Park D, Niewczas M. *Mater Sci Eng A*, 491 (2008) 88–102.
- [46] Park W. S, Seong Won Yoo, Myung Hyun Kim, Jae Myung Lee, *Materials and design* 31 (2010) 3630-3640.
- [47] Petch NJ, Armstrong RW. Work hardening in cleavage fracture toughness. *Acta Metall* 37 (1989) 2279–85.
- [48] Purceka G., Yapicib G.G., Karaman I., Maier H.J., *Materials Science and Engineering A* 528 (2011) 2303–2308.
- [49] Seetharaman V., Krishnan R., *J. Mater. Sci.* 16 (1981) 523–530.
- [50] Simar A, Bre'chet Y, de Meester B, Denquin A, Pardoën T., *Acta Mater* 55 (2007) 6133–43.
- [51] Tatsuro Morita, Kei Hatsuoka, Takashi Iizuka and Kazuhiro Kawasaki, *Materials Transactions*, 46, 7 (2005) 1681 - 1686
- [52] *Titanium a technical guide*, Edited by Matthew J. Donachie, Jr. ASM international (1988) 32-35. ISBN: 0-87170-309-2.
- [53] *Titanium and Titanium Alloys. Fundamentals and Applications*, Edited by Christoph Leyens, Manfred Peters, WILEY-VCH Verlag GmbH & Co. KGaA, Weinheim (2003) pp 333-349
- [54] Tsao L.C., Wub H.Y., Leong J.C., Fang C.J., *Materials and Design* 34 (2012) 179–184.
- [55] Wang Songtao, Yanga, Ke, Shan Yiyin, Laifeng Li, *Materials Science and Engineering A* 490 (2008) 95–104
- [56] Zener C, Holloman JH, *J Appl Phys* 15 (1944) 22–32.
- [57] Zhang B., Mynorsa D.J., Mugarra A., Ostolaza K., *Journal of Materials Processing Technology* 153–154 (2004) 694–698
- [58] Zhang Zhongping, Qiang Sun, Chunwang Li, and Wenzhen Zhao, *Theoretical Calculation of the Strain-Hardening Coefficient and the Strength of Metallic Materials*, ASM International JMEPEG (2006) 15:19-22.

Titanium Aluminides for Metallic Thermal Protection System of Reusable Space Transportation Vehicle: A Review

R.K. Gupta, P. Ramkumar

Materials and Mechanical Entity, Vikram Sarabhai Space Centre, ISRO, Trivandrum, India -695 022

*Corresponding author: Tel +91-0471-2562484, Fax: +91-0471-2705427, rohitkumar_gupta@vssc.gov.in

Abstract

Gamma phase based two phase ($\gamma+\alpha_2$) titanium aluminides have promising potential as high temperature structural materials particularly for aerospace systems due to light weight. They are potential candidate materials for metallic thermal protection system (MTPS) of reentry vehicles. Limitations with respect to processing have been reported due to poor formability below 700°C. However, different specialized techniques have been evolved to realize the material in various forms. The present paper brings out the candidature of this material (two phase $\gamma+\alpha_2$ titanium aluminides) for MTPS and discusses the different processing options. Viable process route is also discussed to obtain thin sheets for MTPS.

Keywords

MTPS; Ti Aluminide; Processing; High Temperature Material

Introduction

In the era of interplanetary space missions, several advanced materials have been designed to achieve a set of targeted mechanical and functional properties. In recent times, low cost access to space has been in focus and accordingly selection of materials for various systems gains much importance. For missions like reusable launch vehicle, damage tolerant material with reusability is one of the important criteria. For thermal protection system, alternate material to ceramic based TPS is being discussed to ensure more reliability, and reusability, and in order to avoid Columbia shuttle type of disaster, metallic thermal protection system is found to be conceptually better option. However, increase in density due to metallic system is being evaluated. Among the available high temperature metallic materials, superalloys have high density. In such scenario, Titanium aluminide (TiAl+ Ti₃Al) is one of the suitable materials, which has low density (~3.8 gm/ cm³) coupled with attractive high temperature properties (upto about 1273K) as compared to superalloys. Among the two types of Ti aluminides (γ & α_2), γ -titanium aluminide (TiAl) has advantage of lower density and higher strength than α_2 -titanium aluminide (Ti₃Al) at elevated temperatures. Further, combination of these two phases ($\gamma+\alpha_2$) results in a good combination of high temperature strength and ductility. This material is envisaged for turbine blades, turbine rotor discs, fins, nozzle, automobile rotor discs, etc.

Room temperature ductility of alloy is very low and therefore alloy modifications and specialized processes are developed to realize the material in different forms. In this paper, properties of Ti aluminide have been compared with various candidate materials for TPS and processing options of Ti aluminide for MTPS are discussed.

Concept of MTPS

The metallic TPS designed earlier called Adaptable, Robust, Metallic, Operable Reusable (ARMOR) thermal protection system is developed by Langley Research Center. The overall TPS panel has dimensions of 457 x 457 x 89 mm. The major components of ARMOR are: an inconel honeycomb panel, a thin gauge titanium box beam frame, stand-off support brackets, four compliant bellows-type tubes, bulges compliant sides, titanium foil closeout and saffil™, a loose alumina fibrous insulation.

The honeycomb panel consists of 0.15 mm thick inconel 617 face sheets brazed to 6.3 mm thick inconel 617

honeycomb cores with 4.7 mm thick cell walls. A coating that simultaneously increases the surface emissivity and provides oxidation protection is applied to the outer face sheet. This coating consists of an alumina base layer and a two-phase glass outer layer with a total thickness of approximately 0.005 mm with an emissivity of 0.86. The inner surface of the metallic box is made of titanium alloy, Ti 6Al-4V.

The honeycomb sandwich is fabricated by brazing process to realize 4.7mm diameter cells. Side walls are formed into their beaded shape with appropriate flanges to form over or underhanging lips and brazed to the inconel honeycomb sandwich. The fastener access tubes and covers are fabricated and brazed to the outer honeycomb sandwich. The lower honeycomb sandwich is diffusion bonded together. Internal insulation is installed and the inconel side walls are brazed to the lower surface of titanium alloy sheet to complete the TPS panel. A photograph of honeycomb is presented in Fig. 1.

With the establishment of conceptual design, fabrication and testing of metallic thermal protection system; studies towards application of high temperature lighter metallic material are being conducted. Ti aluminide has been considered as a prominent candidate and tests at different levels are being conducted to induct this alloy into the system. A brief comparison of MTPS with ceramic TPS is presented in Table 1, and candidature of Ti aluminide in comparison with other high temperature alloys is presented in Table 2. Photographs showing construction of honeycomb panel are presented in Fig. 2.

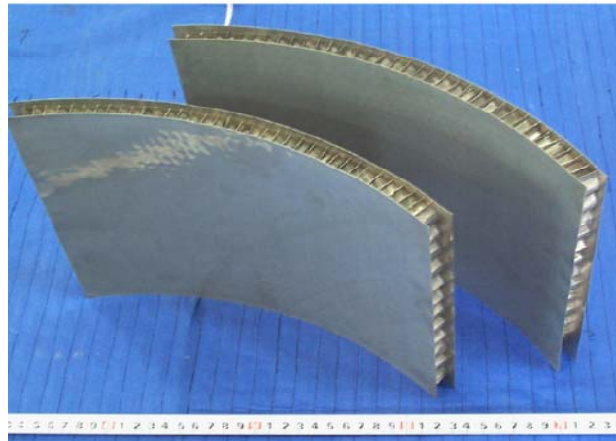


FIG. 1: PHOTOGRAPH SHOWING HONEYCOMB PANEL

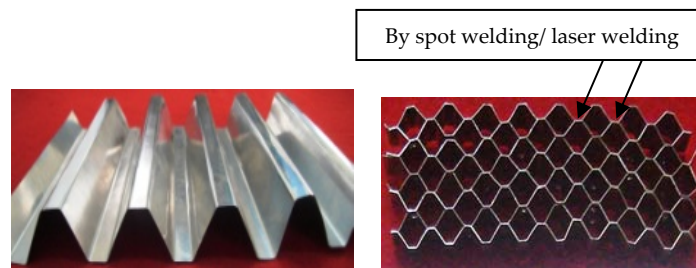


FIG. 2: PHOTOGRAPHS SHOWING HONEYCOMB CONSTRUCTION OF SUPERALLOY/ TiAl PANEL

Processing Methods of Aluminides

High melting point of aluminides and their ordered structure make the alloy brittle at ambient temperature [1, 9, 10]. The problem of poor ductility has been addressed to some extent by alloy design and processing. However, difficulties in conventional processing are experienced and therefore different processing techniques have been evolved over the years. Primary processes can be grouped into two categories viz. casting/ingot-metallurgy route and powder metallurgy (PM) route.

Primary Processing

The titanium aluminides with maximum ductility at room temperature, which is of potential interest have

composition of 45-50 at% Al. This alloy solidifies with peritectic reaction, which results in segregation and non-uniform structures. Alloying additions minimize the segregation and improve castability. Further to minimize the segregation-related problems, advanced melting techniques like electron beam melting (EBM), plasma arc melting (PAM) and vacuum arc remelting (VAR) have been attempted (Fig. 3). Large ingots of 360 mm diameter, weighing 250 Kg have been produced commercially. Rapid solidification has also been used to minimize the segregation. However, risk of contamination during processing by rapid solidification could not be ruled out.

In powder metallurgy (PM) route, there are basically two approaches based on pre-alloyed and elemental-powder processing techniques. Pre-alloyed PM route poses problems of coarse grains, cracking and porosity. However, microstructures and properties comparable to those of wrought products have been achieved through hot isostatic pressing. Elemental PM Route is attractive due to the above problems encountered in pre-alloyed powder processing. Reaction synthesis (RS) process, which uses heat of reaction of elemental powders, is a potential method for producing aluminides. Many variants of RS process namely reactive hot pressing, combustion synthesis, reactive hot isostatic pressing, reactive extrusion, etc. have been studied. The process involves a transient liquid between the powder particles for a small duration and in small amount depending on process parameters. To minimize Kirkendall porosity and oxidation, to improve densification and to obtain stable intermetallic phases; process parameters like particle size, heating rate, atmosphere, temperature, time and external pressure are optimized.

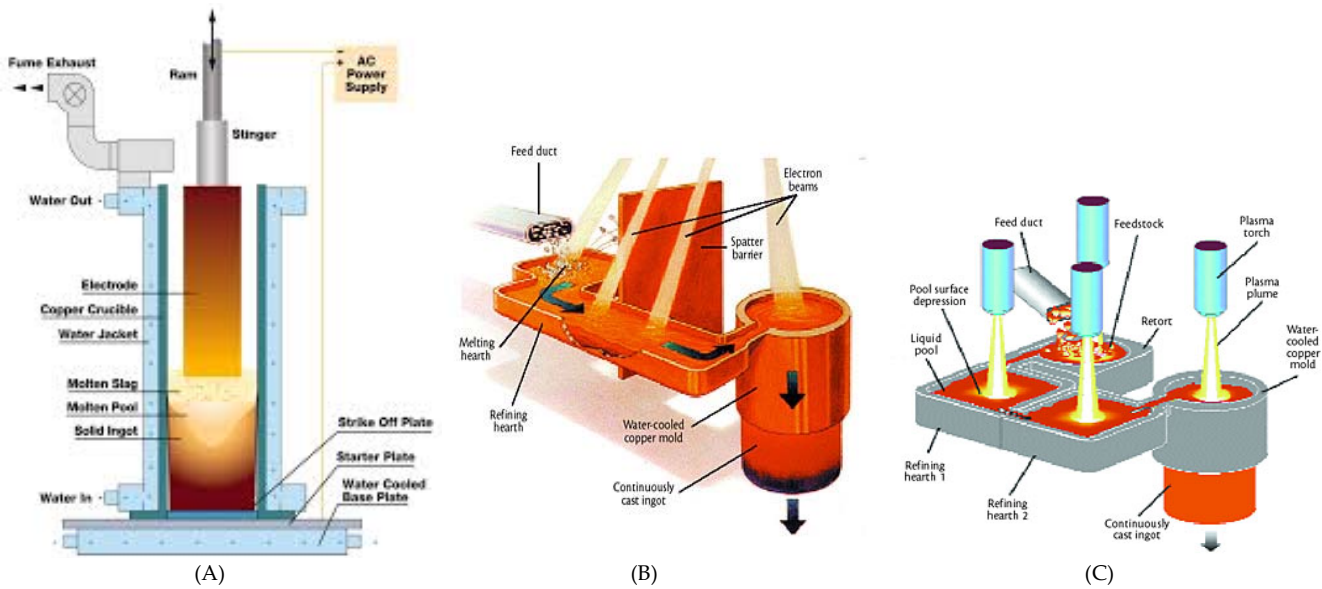


FIG. 3: PHOTOGRAPHS SHOWING VARIOUS MELTING PROCESSES, A. VAR, B. EBM, C. PAM

TABLE 1: COMPARISON BETWEEN CERAMIC AND METALLIC SYSTEMS

SI No	Property	Ceramic Tiles	Metallic TPS
1	Insulation	Very Good	To be proven in flight
2	Integration	Time Consuming	Less Time
3	Turn Around time	Long	Short
4	Maintenance	Complicated	Less
5	Water proofing	After every flight	Not required
6	Coating	Easy	Selection of functionally gradient coating (FGC) to take care of expansion mismatch
7	Cost	High	Relatively less
8	Weight	Lightweight	Comparatively more
9	Integration	Bonding	Fasteners

Mechanical alloying (MA) has also been studied to generate metastable crystalline or amorphous phases. However, MA process has difficulty of secondary consolidation as the powders are in heavily worked condition. Microwave RS process can result in better intermetallic products as the heating rates involved are high.

In Ti-Al system, swelling takes place for pressure-less reaction synthesis due to solubility imbalance. However, use of pressure during reaction sintering can lead to dense products in Ti-Al system and has been used to produce near-net shape gamma TiAl. Thin foils of 50 μ m thickness from reaction extruded TiAl have been realized, which is an achievement for difficult to roll aluminides.

TABLE 2: COMPARISON OF DIFFERENT METALLIC MATERIALS FOR MTPS

Property	Ti base	Ti ₃ Al base	TiAl base	Superalloy
Structure	HCP/BCC	DO ₁₉	L1 ₀	FCC
Density, g/cc	4.5	4.1-4.7	3.7-3.9	8.3
Modulus, GPa	95-115	110-145	160-180	206
YS, MPa (RT)	380-1150	700-990	450-600	900
UTS, MPa (RT)	480-1200	800-1140	750-950	1000
% El at RT	10-25	1-5	1-4	5-10
% El at HT	12-50	10-20	10-30	10-20
K1c, MPa(m) ^{0.5}	45-55	13-30	10-25	25
Creep limit (K)	873	1033	1273	1363
YS, MPa (973K)	-	450-500	450-600	800
UTS, MPa (973K)	-	600-750	750-950	950

Secondary Processing

Microstructures of Ti-Al products play significant role in determining their mechanical properties, which can be optimized/ modified through mechanical working and appropriate heat treatment. It is found that major challenge of the wrought processing is to break down the coarse and segregated structure of the cast ingots. Safe working zone (temperature and strain rate) can be identified. Isothermal forging is essentially required for processing of these aluminides in the absence of which canned near-isothermal forging or canned extrusion process is adopted. Scientists at the Institute for Metal Superplasticity Problems, Russia have developed a dynamic recrystallisation process based on repeated isothermal forging at progressively low temperatures. This process has resulted in fine-grained aluminides that sustain large deformations without cracking. Subsequently, thin sheets and foils have been realized by pack rolling techniques.

Heat treatment of aluminides is carried out at different temperatures to obtain desired microstructures. Wang et al. successfully refined the coarse lamellar microstructure of 500 μ m to 10 μ m by rapid heat treatment. By varying the heating temperatures and cooling rate from α -transus temperature, various combinations of mechanical properties and microstructures can be obtained as per requirement.

Another important aspect in component realization is cutting and machining of aluminides, which requires electro discharge machining (EDM). Many a time workpiece surface disintegrity and tool breaking problems have been reported and therefore cutting/ machining is carried out by EDM or by water jet process.

Discussions

Difficulties associated with IM route are elemental segregation, elemental loss, non-homogenous structures, cracking and requirement of secondary working to produce useful parts. Specialized techniques like VAR, EBM and PAM also have small elemental loss through evaporation. However, these are the only techniques for processing of large size ingots. There are some definite advantages for PM processes like fine grain size of product, near net shape processing, material saving and controlled properties. RS processes have benefits like simplicity with low energy requirements, possibility of obtaining high purity products, simultaneous formation, densification and near-net shape processing. This route results in finer structures with more homogeneity and with metastable phases. However, PM process has the biggest limitation in terms of processing of larger size ingots/ billets for bigger products.

Near net shape processing through direct casting/ investment casting and reaction synthesis are promising processing techniques for actual component fabrication. Both cast and wrought alloys have been studied for their deformation behavior and specialized process based on isothermal processing like pack forging/ rolling has been

suggested.

Summary

Among various MTPS material, γ -Ti aluminide based two phase ($\gamma+\alpha_2$) Ti aluminide is found to be a potential alternative due to its high temperature properties coupled with low density. Earlier difficulties in development of Ti aluminides and processing have been overcome with alloy design and innovative processing methods. Billets can be made through ingot metallurgy route employing VAR process and then near isothermal processing like pack forging/ rolling can be adopted to get required size of Ti aluminide products. In line with the design of ARMOR, MTPS can be developed with the Ti aluminide sheets/ foils (for honeycomb) in combination with other alloys like Ti6Al4V. Further, alloy design is another area to improve the workability of the alloy and is being attempted with the addition of Nb like elements.

ACKNOWLEDGEMENT

Author thanks Director, VSSC for permitting to publish this work.

REFERENCES

- [1] Appel F., Oehring V and Wagner V., *Intermetallics*, 8 (2000) 1283.
- [2] Beschliesser M., Chatterjee A., Lorich A., Knabl W., Kestler H., Dehm G., Clemens H., *Mater.Sci. and Engg. A329-331* (2002) 124.
- [3] Bose A., Rabin B. H. and German R. M., *P M Int*, 20 (1988) 25.
- [4] Chen G.L., Xu X.J., Teng Z.K., Wang Y.L., Lin J.P., *Intermetallics* 15 (2007) 625.
- [5] Christman T. and Jain M. *Scr Met Mater*, 25 (1991) 767.
- [6] Clemens H., Bartels A., Bystrzanowski S., Chladil H., Leitner H., Dehm G., Gerling R., Schimansky F. P., *Intermetallics* 14 (2006) 1380.
- [7] Das Gopal; Kestler H.; Clemens H and Bartolotta P.A. *JOM*, 56, 11 (2004) 42.
- [8] German R. M., *Advances in P M*, 2 (1990), 115.
- [9] German R. M., Bose A., and Stoloff N. S., *High Temp Ordered Intermetallic Alloys III*, Eds Liu C. T., Taub A.I., Stoloff N.S. and Koch C. C., *MRS Proc*, 133 (1989)403.
- [10] German R. M., *Liquid Phase Sintering*, Plenum Press (1985) NY.
- [11] Guther V., Otto A., Kestler H., Clemens H., *Gamma Titanium Aluminides 1999*, ed. Kim Y.W., Dimiduk D.M., Loretto M.H., TMS Warrendale, PA, USA, 1999, 225.
- [12] Huang S. C. and Chesnutt J. C., *Intermetallic Compounds*, Eds Westbrook J. H. and Fleisher R. L., John Wiley and Sons, 2 (1994) 73.
- [13] Huang S. C. and Siemers P. A. *Met Trans 20A* (1989) 1899.
- [14] Imayev R. M., Gabdullin N. K., Salishchev G. A., Senkov O. N., Imayev V. M., Froes F. H., *Acta Mater.* 47 (6) (1999) 1809.
- [15] Imayev R. M., Imayev V. M. and Salischev G., *Scr Met Mater*, 29 (1993) 713.
- [16] Imayev R. M., Imayev V. M. and Salischev G., *Scr Met Mater*, 29 (1993) 719.
- [17] Imayev R. M., Kaibyshev O. A., Salishchev G. A., *Acta Met.* 40 (3) (1992) 581.
- [18] Imayev V., Imayev R., Kuznetsov A., *Scripta Mater.* 49 (2003) 1047.
- [19] Kim J. K., Kin T. K., Lee T. K., Hwang S. K., Nam S. W. and Kim N. J. *Gamma Ti Aluminides*, Eds Kim Y. W., Dimiduk D. M. and Loretto M. H., *The Minerals, Metals and Material Society*, (1999) 231.
- [20] Kim Y. W. *JOM*, 46, (7) (1995) 39.
- [21] Koch C. C., *Int Mater Rev*, 33, (4) (1988) 201.
- [22] Lee T. K., Mosunov E. I. and Hwang S. K. *Mater SciEng*, A239-240 (1997) 540.

- [23] Lipsitt H. A., High Temp Ordered Intermetallic Alloys, Eds Koch C. C., Liu C. T. and Stoloff N. S., MRS, 39 (1985) 351.
- [24] Martin P. L. and Hardwick D. A., Intermetallic Compounds, Eds J. H. Westbrook and R. L. Fleisher, John Wiley and Sons, 1 (1994) 637.
- [25] Martin P. L., Mendiratta M. G. and Lipsitt H. A., Met Trans, 14A (1983) 2170.
- [26] Max L. Blosser, Development of Metallic Thermal Protection Systems for the Reusable Launch Vehicle, NASA Technical Memorandum 110296, 1996.
- [27] Mckamey C. G., Whang S. H., and CT Liu, Scr Met Mater, 32, (3) (1995) 383.
- [28] Mohan B., Rajadurai A. and Satyanarayana K. G., JMater Processing Tech, 153-154 (2004) 978.
- [29] Munir Z. A. and Anselmi - Tamburini, Mater Sci Rep, 3 (1989) 277.
- [30] Nakagawa Y. G., Yokoshima S. and Mastuda K. Mater SciEng A, 153 (1992) 722.
- [31] Nishimura C. and Liu C. T., Acta Met et Mater, 41 (1993)113.
- [32] Nishiyama Y., Miyashita T., Isobe S. and Noda T. High Temp Aluminides and Intermetallics, Eds S. H. Whang, Liu C. T., Pope D. P. and Steigler J.O., The Minerals Metals and Mater Society, USA (1990) 557.
- [33] Prasanth N, Pillai R. M. and Pai B. C., Indian Foundry Journal 50(1) (2004) 50.
- [34] Qiuming Zhang, Xiaodong He, Mater. Characterization 60 (2009) 178.
- [35] R. K. Gupta, Bhanu Pant, Vijaya Agarwala, R. C. Agarwala and P. P. Sinha, High Temperature Mater. And Processes 28 (3) (2009) 121.
- [36] R. K. Gupta, Bhanu Pant, Vijaya Agarwala, R. C. Agarwala and P. P. Sinha, Journal of Mater Sci. and Tech. In press.
- [37] R. K. Gupta, Vijaya Agarwala, Sunayan Thakur, R. C. Agarwala, Bhanu Pant, Advanced Mater. Res. 67 (2009) 45.
- [38] Rawers J. C. and Wrzesinky, W. R. J Mater Sci , 27 (1992) 2877.
- [39] Salischev G., Imayev R M., Senkov O. N., and Froes F. H., JOM, Dec. (2000)46.
- [40] Salischev G., Imayev R M., Senkov O. N., Imayev V. M., Gabdullin N. K., Shagiev M. R., Kuznestov A. V. and Froes F. H., Mater SciEng, A286 (2000) 236.
- [41] Savstkii A. P. and Brutsev N. N., Soviet P M Metal Ceramics, 20 (1981) 681.
- [42] Savstkii A. P., Soviet P M Metal Ceramics, 19 (1980) 488.
- [43] Seetharaman V., Semiatin S. L., Mater.Sci. and Engg. A299 (2001) 195.
- [44] Semiatin S. L. and Mcquay P. A. Met Trans A, 23A (1992) 149.
- [45] Semiatin S. L., Vollmer D. C., El-Soudani S., Su C., Scripta Mater. 53 (1990) 1409.
- [46] Sharman A.R.C., Aspinwall D.K., Dewes R.C., Bowen P., Wear 249 (2001) 473.
- [47] Sikka V. K., High Temp Aluminides and Intermetallics, Eds Whang S. H., Liu C. T., Pope D. P. and Stiegler J. O., TMS, Warrendale (1990) 505.
- [48] Srinivasan S., Desch P. B. and Schwartz R. B. Scr Met Mater, 25 (1991) 2513.
- [49] Suryanarayana C., Froes F. H. and Riowe R. G., Int Mater Rev, 9 (11) (1990) 948.
- [50] Taub A. I. and Fleischer R. L. Science, 243 (1989) 616.
- [51] Tetjukhin V.V., Levin I.V., Kozlov A.N., Poljanskij S.N. (2002), US Patent No. 2179899 dated 9 Apr 2002.
- [52] Tetsui T., Intermetallics, 10 (2002) 239.
- [53] Tetsui T., Mater SciEng, A329-331 (2002) 582.
- [54] Venskutonis A. and Kibacher K., European Space Agency Bulletin, 10 (2000) 2.
- [55] Vujic D., Z. Li and S. H. Wang, Met Trans A, 19A (1988) 2445.
- [56] Wang J. N., Yang J., Wang Y., Scripta Mater. 52 (2005) 329.
- [57] Wen C. E., Yasue K. and Yamada Y. J Mater Sci, 36 (2001) 1741.
- [58] Yao C., Lü H., Jia Z., Jia X., Lu Y., Li H., Acta Astronautica 63 (2008) 280.
- [59] Zhang W., Liu Y., Li H.Z., Li Z., Wang H., Liu B., J. of Mater. Process. Techno. 209 (2009) 5363.

DNS of Low Reynolds Number Aerodynamics in the Presence of Free Stream Turbulence

P. M. Bagade^{*1}, S. B. Krishnan², T. K. Sengupta³

Department of Aerospace Engineering, Indian Institute of Technology Kanpur, India

^{*}pmbagade@iitk.ac.in; ²sathishbkrishnan@gmail.com; ³tksen@iitk.ac.in

Abstract

Here, Direct Numerical Simulation (DNS) of low Reynolds number (Re) flow in the presence of free stream turbulence (FST) pertaining to micro-aerial vehicle (MAV) is reported. The focus is on numerically simulating the flow around an airfoil at low Re to understand its behaviour using high accuracy compact schemes (T. K. Sengupta, *High Accuracy Computing Methods*, Cambridge University Press, New York, 2013.) [1]. In low Re aerodynamics, the flow is characterized by unsteady separation bubbles and vortex shedding from the suction surface and the trailing edge as well, which make it different from high Re aerodynamics. The maximum attainable lift coefficient and lift-to-drag ratio decreases drastically at low Re , as compared to high Re flows. Such flows are also important because of their susceptibility to background disturbances. Stalling of aircraft wing is one such phenomenon where free stream turbulence (FST) plays a crucial role. In this work, effects of FST, effects of Re and angles of attack α are studied with respect to flow separation and vortex shedding. Flow characterization is done for the AG24 airfoil, at $Re = 60,000$ and $400,000$, with and without consideration of FST in the range of angles of attack, $-6^\circ \leq \alpha \leq +6^\circ$. The computational results are compared with the experimental results of Williamson et al. (*Summary of Low Speed Airfoil Data*, volume 5, Dept. of Aerospace Engineering, UIUC, 2007) [2] and are found to be in good agreement. Flow simulation over AG24 airfoil is performed here via parallel computation, using high accuracy compact schemes for spatial discretization and optimized Runge-Kutta (ORK₄) scheme for time marching [1]. This paper also discusses proper implementation of filters and FST model.

Keywords

Direct Numerical Simulation; MAV; AG24 Airfoil; High Accuracy; Numerical Schemes; Low Reynolds Number Aerodynamics

Introduction

The low speed aerodynamics is significantly different from that of conventional aircraft aerodynamics, because of low chord-based Re , as in case of MAV [3, 4, 5]. Such flows are characterized by unsteady separation bubble formation and intense vortex shedding from the trailing edge and the suction surface, so that the maximum attainable lift and the lift-to-drag ratio comes down, reducing the aerodynamic performance. The biggest hindrance in the development of a fully functional and aerodynamically adept MAV is lack of understanding for low Re flow regime [6, 7]. Owing to the unsteadiness of flow, experimental works become particularly difficult for such low Re regimes. This makes computational simulations comparatively more viable and reliable. Proper computational studies have also been hindered due to difficulties in resolving space-time scales accurately. Here, we have tried to resolve this difficulty with the aid of high accuracy compact schemes [1]. The same schemes have been used in [49] for direct numerical simulation of transitional flows over a NLF airfoil. The presence of unsteady separation bubbles plays a pivotal role in dictating the aerodynamic performance, because of which the airfoil/wing performance tends to be lower for low Re flows [8]. However at higher Re , the shear layer undergoes transition to turbulence while remaining attached to the airfoil surface, hence suppressing the bubble formation and improving aerodynamic performance. It is only at higher angles of attack for high Re that the formation of short bubbles is seen, which however has little impact on overall flow physics. Separation zones are of particular importance in relation to the airfoil boundary layer. The location and extent of these regions depend on flow speed, angle of attack, presence of background disturbances and their intensity.

The phenomena of separation and transition are highly sensitive to Re , pressure gradient and the disturbance environment which play a critical role in determining the boundary layer development. The flow, which is initially laminar, separates due to adverse pressure gradient. The separated shear layer undergoes transition to a turbulent

state which then reattaches on to the airfoil surface, resulting in a laminar separation bubble (LSB) between the zones of separation and reattachment. Also, since MAV flight occurs in atmospheric boundary layer, it is always affected by eddies of different scales in FST. It was shown by Mueller [9] that an increase in FST intensity reduces the minimum drag and slightly increases the maximum attainable coefficient of lift, C_L . It was also found experimentally that at higher angles of attack, where the flow is separated, increase in turbulence intensity results in an increase in drag. Hence, proper selection and implementation of accurate FST model is imperative to understand flow physics.

Influence of FST on low Re flows was studied by Pohlen [10], using a 13% thick Miley airfoil [11] and reported that the effect of turbulence reduces the hysteresis. He also showed an increase in airfoil performance aided by FST. The extent of LSB depends on angle of attack, camber and inversely depends on flow speed. These regions of reverse flow also show large fluctuations in drag values. The smaller, short bubbles affect only the local pressure distribution and contribute little towards the overall aerodynamics. However, these might burst, forming longer bubbles or even an unattached free shear layer, either of which alters the flow globally. In extreme cases, this results in loss of lift, and may cause stall on the airfoil [12, 13]. The authors in [12, 13] also observed that these LSBs are inherently unstable, being highly sensitive to the turbulence intensity of FST, acoustic waves, pressure gradient etc. Presence of strong adverse pressure gradient results in periodic vortex shedding from the bubble [14]. Burgmann [15] showed that separated shear layer of long bubbles are governed by Kelvin-Helmholtz instabilities due to stronger velocity gradient normal to the airfoil surface.

Pressure distribution over the airfoil surface, given by the C_p plot is also a good indicator of the presence and extent of LSB. Owing to large fluctuations in force, the regions of large deviations in the pressure over the airfoil are due to the reattachment phenomenon [16, 17]. In the Re range of 1000 to 10,000, the flow is laminar and it does not suffer transition. The Re range of 30,000 to 70,000 is of critical interest since the flow is highly sensitive on the choice of airfoil, with thickness of 6% and more showing hysteresis due to laminar separation with transition. It is noted in [18] that the separation bubble shows unsteady phenomena like flapping of the boundary layer reattachment and periodic bursting of short bubbles, all of these resulting in fluctuation of aerodynamic forces and thus affecting the airfoil performance leading to buffeting and stalling. However, in the presence of FST the flow is altered qualitatively. Earliest of these studies was done using grid induced turbulence [19], showing that with increase in FST, stall angle increases [20]. Studies done using NACA airfoil showed good match with the findings in [20], and in addition it also reported an increase in the maximum value of C_L [21]. Studies done by Swalwell [22] showed a delay in stall and increase in maximum lift coefficient with increase in FST. It was also shown that with increase in FST, the size of LSB decreases along with an increase in the maximum C_p [23, 24, 25]. Studies conducted by Cruz [26] and Loxton [27] also indicated that with increasing FST, stall angle increases along with the aerodynamic performance. It is seen that the flow is largely dictated by the non-linear mechanisms and this along with the unsteady nature of flow makes it increasingly difficult to resolve the flow features accurately. Though a lot of ambiguity still exists about the low speed flow properties, transition is believed to take place through amplification of disturbances within the shear layer. Instabilities amplify within the detached shear layer to form coherent structures, which re-energize the boundary layer, causing transition to turbulence [28]. However, it cannot be assured that the increase in FST would improve the performance, since increasing thickness of turbulent boundary layer also result in an increase in drag and thus affect the L/D adversely. Thus, it is imperative to study low Re flows and understand the flow features.

Governing Equations and Numerical Formulation

The time-accurate flow field around airfoil is obtained by solving Navier-Stokes equation (NSE) following the methodology described in [1, 29], with appropriate initial and boundary conditions. The governing equations of motion for the 2D flow are given by the NSE in stream function and vorticity (ψ, ω) - formulation given by

$$\nabla^2 \psi = -\omega \quad (1)$$

$$\frac{\partial \omega}{\partial t} + \nabla(\omega V) = \frac{1}{Re} \nabla^2 \omega \quad (2)$$

where, $Re = U_\infty c / \nu$, U_∞ being the free-stream speed, c is the airfoil chord and ν is the kinematic viscosity. The (ψ, ω) - formulation is used for higher accuracy, which satisfies the solenoidal condition for velocity and vorticity fields simultaneously. Existence of stream function satisfies mass conservation in full domain and thereby removes errors caused in primitive variable formulations. Also, such computation becomes faster as pressure is not computed explicitly, since it is the application of pressure boundary condition that gives rise to more problems than the vorticity boundary conditions [1]. It is the vorticity dynamics which dictates flow evolution. Equations (1) and (2) are solved in an orthogonal transformed plane. The NSE in an orthogonal transformed plane are as follows [1, 29]

$$\frac{\partial}{\partial \xi} \left(\frac{h_2}{h_1} \frac{\partial \psi}{\partial \xi} \right) + \frac{\partial}{\partial \eta} \left(\frac{h_1}{h_2} \frac{\partial \psi}{\partial \eta} \right) = h_1 h_2 \omega \quad (3)$$

$$h_1 h_2 \frac{\partial \omega}{\partial t} + h_2 u \frac{\partial \omega}{\partial \xi} + h_1 v \frac{\partial \omega}{\partial \eta} = \frac{1}{Re} \left[\frac{\partial}{\partial \xi} \left(\frac{h_2}{h_1} \frac{\partial \omega}{\partial \xi} \right) + \frac{\partial}{\partial \eta} \left(\frac{h_1}{h_2} \frac{\partial \omega}{\partial \eta} \right) \right] \quad (4)$$

The contra-variant components of the velocity vector are given by

$$u = \frac{1}{h_2} \frac{\partial \psi}{\partial \eta} \quad (5)$$

$$v = \frac{1}{h_1} \frac{\partial \psi}{\partial \xi} \quad (6)$$

where h_1 and h_2 are scale factors of the transformation in azimuthal (ξ) and wall-normal directions (η) respectively, given by $h_1 = \sqrt{x_\xi^2 + y_\xi^2}$ and $h_2 = \sqrt{x_\eta^2 + y_\eta^2}$. Equations (3) and (4) are the stream-function equation (SFE) and vorticity transport equation (VTE) in the transformed plane respectively. The pressure field is obtained numerically by solving the governing pressure Poisson equation (PPE) for the total pressure P_t , given in the orthogonal coordinate system as [1, 29],

$$\frac{\partial}{\partial \xi} \left(\frac{h_2}{h_1} \frac{\partial P_t}{\partial \xi} \right) + \frac{\partial}{\partial \eta} \left(\frac{h_1}{h_2} \frac{\partial P_t}{\partial \eta} \right) = \frac{\partial(h_2 v \omega)}{\partial \xi} - \frac{\partial(h_1 u \omega)}{\partial \eta} \quad (7)$$

Figure 1 shows schematic of the flow domain with initial and boundary conditions indicated. At the airfoil surface, the no-slip boundary condition is set and we set $\psi_{wall} = Constant$ for the solution of SFE. Wall vorticity is calculated

by $\omega_{wall} = -\frac{1}{h_2^2} \frac{\partial^2 \psi}{\partial \eta^2}$ which uses the no-slip condition. At the inflow, without considering FST effect, free stream

conditions obtained from potential flow solution is applied, by which $\frac{\partial \psi}{\partial y} = U_\infty(t)$. Convective boundary condition

is used on radial velocity at the outflow on the outer boundary. This boundary condition is given by [30]

$$\frac{\partial \omega}{\partial t} + u_c(\xi, \eta, t) \frac{\partial \omega}{\partial \eta} = 0 \quad (8)$$

Periodic boundary condition is applied for all variables on $\xi = constant$ line emerging from the leading edge, where grid cut is positioned. To solve the PPE, the required Neumann boundary condition on the physical surface and in the far-field are obtained from the normal (η) momentum equation given by

$$\frac{h_2}{h_1} \frac{\partial p}{\partial \eta} = -h_1 u \omega + \frac{1}{Re} \frac{\partial \omega}{\partial \xi} - h_1 \frac{\partial v}{\partial t} \quad (9)$$

Thus, the solution of PPE provides the total pressure, P_t , which is the static pressure on the no-slip wall. Further, the coefficients of lift, drag and pitching moment are derived from this to obtain the lift curve and drag-polar. The region $n_2 - n_1$ of the Figure 1 is the inflow domain without considering FST and the region $n_1 - n_2$ is the outflow

domain. However, when introducing FST we also introduce a point n_1' before n_1 and a point n_2' after n_2 , such that the region $n_2' - n_1'$ is the inflow domain and the region $n_1 - n_2$ is the outflow domain, with the region in between, namely $n_1' - n_1$ and $n_2 - n_2'$ acting as buffer zones permitting smooth variation from FST inflow condition to Sommerfeld outflow condition.

Grid Generation

To obtain a good time-accurate solution of the flow, a good quality mesh is a pre-requisite. Though there have been many recent advances in mesh-free methods for flow analysis, the feasibility and applicability is not very universal [31, 32]. A good quality grid generation should ensure smooth grid metrics with no shocks and should give a fine control on grid spacing in all the directions. It should also be able to eliminate or minimize errors due to flow distortion and aliasing [29].

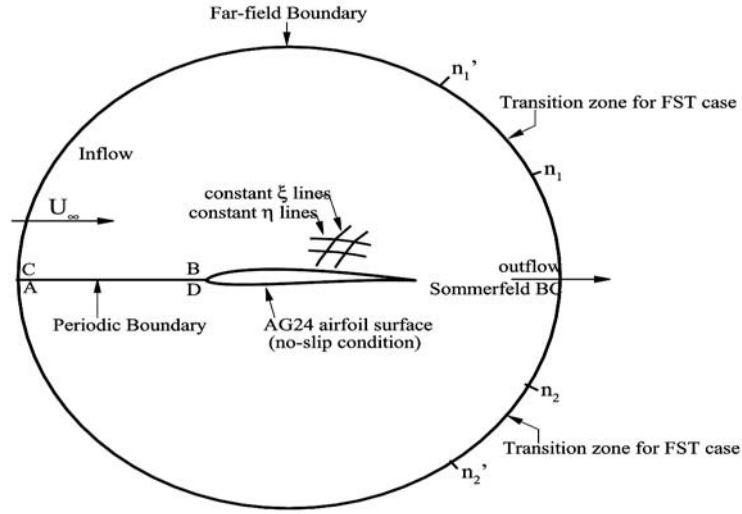


FIG. 1 SCHEMATIC OF THE COMPUTATIONAL DOMAIN WITH GRID LINES AND BOUNDARIES REPRESENTED.

Finite difference methods requires mapping of non-uniformly spaced points in physical plane, (x,y) -plane, to uniformly spaced points in transformed plane, (ξ,η) -plane, by the relations $x = x(\xi,\eta)$ and $y = y(\xi,\eta)$, i.e., every point in the physical plane is a linear scalar function of a particular point in the transformed plane governed by the following equations [1, 29]

$$\nabla^2 x = 0; \nabla^2 y = 0 \quad (10)$$

Orthogonality is maintained by satisfying the relation

$$x_\xi x_\eta + y_\xi y_\eta = 0 \quad (11)$$

Strict condition of orthogonal mapping is required to maintain the uniqueness and this requires a strict definition of the scale functions [29, 33, 34] as $h_1 = \sqrt{x_\xi^2 + y_\xi^2}$ and $h_2 = \sqrt{x_\eta^2 + y_\eta^2}$, which helps defining the distortion function

$$f = \frac{h_2}{h_1} \quad (12)$$

Using the definitions of scale factors we get the following Beltrami equations [29, 34-36] for general orthogonal mapping

$$x_\xi = -f y_\eta \quad (13)$$

$$x_\eta = f y_\xi \quad (14)$$

The grid is generated following a procedure which is a variation of that is given in [29]. We use Equation (11) and one of the Beltrami Eqs. (13) and (14) [33], to obtain an orthogonal grid. A stretching is specified in the wall-normal

direction as

$$\Delta S_\eta = H \left[1 - \frac{\tanh[\beta(1-\eta)]}{\tanh[\beta]} \right] \quad (15)$$

With β a clustering parameter and ΔS_η represents the grid-line increment in η – direction and H is the distance of the outer boundary, non-dimensionalized with respect to c . In the present work, we have used a grid with 528 points in the ξ – direction and 497 points in the η – direction.

Numerical Methods and Filters

The numerical solution of NSE is obtained using stream function - vorticity (ψ, ω) formulation. Optimized Upwind Compact Scheme (OUCS3) [29, 37] is used to discretize the nonlinear convection terms in Eq. (4), for its spectral-like accuracy. The VTE is time-advanced using four stage, optimized Runge-Kutta time integration scheme (OCRK₃) [38], while the diffusion terms are discretized in self-adjoint form, using second order central difference scheme.

Discretization of Stream Function Equation

The LHS terms appearing in SFE are discretized using second order central difference scheme represented by

$$\begin{aligned} \frac{\partial}{\partial \xi} \left(\frac{h_2}{h_1} \frac{\partial \psi}{\partial \xi} \right) &= \frac{1}{\Delta \xi^2} \left[\left(\frac{h_2}{h_1} \right)_{i+1,j} \psi_{i+1,j} - \left\{ \left(\frac{h_2}{h_1} \right)_{i+1,j} + \left(\frac{h_2}{h_1} \right)_{i-1,j} \right\} \psi_{i,j} + \left(\frac{h_2}{h_1} \right)_{i-1,j} \psi_{i-1,j} \right] \\ \frac{\partial}{\partial \eta} \left(\frac{h_1}{h_2} \frac{\partial \psi}{\partial \eta} \right) &= \frac{1}{\Delta \eta^2} \left[\left(\frac{h_1}{h_2} \right)_{i,j+1} \psi_{i,j+1} - \left\{ \left(\frac{h_1}{h_2} \right)_{i,j+1} + \left(\frac{h_1}{h_2} \right)_{i,j-1} \right\} \psi_{i,j} + \left(\frac{h_1}{h_2} \right)_{i,j-1} \psi_{i,j-1} \right] \end{aligned}$$

This discretized expression written down for the unknown nodes results in system of linear algebraic equations given by, $[M]\{\psi\} = -\{h_1 h_2 \omega\}$. The matrix M is solved iteratively using pre-conditioned Bi-CGSTAB method [39]. Use of central scheme preserves the isotropy of diffusion and ensures diagonal dominance of the system and maintains M matrix positive definite.

Spatial Discretization of Convection Terms in Vorticity Transport Equation

The convection terms in VTE discretized by OUCS3 scheme provides higher accuracy and aliasing is controlled considerably. In this scheme, derivatives are calculated implicitly, for which one requires special stencils for near-boundary points. Explicit relations are used in non-periodic cases at $j=1$ and 2 as

$$f'_1 = \frac{1}{h} (-3u_1 + 4u_2 - u_3) \quad (16)$$

$$f'_2 = \frac{1}{h} \left[\left(\frac{2\beta_1}{3} - \frac{1}{3} \right) u_1 - \left(\frac{8\beta_1}{3} - \frac{1}{3} \right) u_2 + (4\beta_1 + 1) u_3 - \left(\frac{8\beta_1}{3} - \frac{1}{6} \right) u_4 + \frac{2\beta_1}{3} u_5 \right] \quad (17)$$

where β_1 , is a constant used to stabilize computations and improve dispersion relation preservation of the numerical scheme. The stencils for $j = N-1$ and $j=N$ are similar to the stencils for $j=2$ and $j=1$, respectively. For the inner points ($3 \leq j \leq N-2$), following implicit equations are used

$$p_{j-1} f'_{j-1} + f'_j + p_{j+1} f'_{j+1} = \frac{1}{h} \sum_{n=2}^2 q_n f_{j+n} \quad (18)$$

where, $p_{j\pm 1} = D \pm \frac{\eta_1}{60}$; $q_{j\pm 2} = \pm \frac{F}{4} + \frac{\eta_1}{300}$; $q_{j\pm 1} = \pm \frac{E}{2} + \frac{\eta_1}{30}$; $q_0 = -\frac{11\eta_1}{150}$; $D = 0.3793894912$; $E = 1.57557379$ and

$F = 0.183205192$. Here, a fourth order diffusion is added explicitly, rather than implicitly by using $\eta_1 = 0.06$.

Time Integration Scheme

VTE is time advanced using OCRK3 technique [40], which has superior dispersion relation preservation properties. After spatial discretization, VTE can be represented as, $\frac{\partial u}{\partial t} = L(u)$ where u represents the unknown. To advance from u^n to u^{n+1} , the following steps/stages are carried out in one time step of OCRK3.

$$u^{(1)} = u^{(n)} + a\Delta t L(u^{(n)}) \quad (19)$$

$$u^{(2)} = u^{(n)} + b\Delta t L(u^{(1)}) \quad (20)$$

$$u^{(3)} = u^{(n)} + \Delta t L(u^{(2)}) \quad (21)$$

$$u^{(n+1)} = u^{(n)} + \frac{\Delta t}{6} (L(u^n) + 2L(u^{(1)}) + 2L(u^{(2)}) + L(u^{(3)})) \quad (22)$$

where $a=0.259674099$ and $b=0.499969$ are the optimized values [40].

Filters

Any discretization scheme, while evaluating derivatives, imposes a filter of its own on the unknown [1]. However additionally specific low-pass filters are applied explicitly to remove high wavenumber components from the solutions, removing numerical instability problems. Implicit filters are used here, with the real part of the transfer function [1] as the low-pass filter and the imaginary part attenuates the signal further via additional diffusion which also changes dispersion property of the basic scheme. Here, 1D upwind non-periodic filter [41] is used in ξ – direction, close to the airfoil, as well as, near the outer boundary, with a filtering coefficient, $\alpha_1 = 0.45$. A 2D filter is also used [41, 42], to control aliasing. The coefficient of 2D filtering is equal to 0.24 here and used in adaptive manner [41], where there is a dominant presence of high wave number components.

Free Stream Turbulence Modelling

In most of practical applications, the flow is unsteady, with varying intensities of turbulence. For any applications, the source of these background noises may be acoustic, vortical or entropic in origin. It is noted that solving NSE using moving average model of FST [44, 45] is relevant than solving a stochastic differential equation for laminar flow [46]. Skewness is assumed to be zero for this model [44] and the parameters of the model are fixed by comparing the second and fourth moments of the histogram, which is experimentally obtained [47], with that of the model. From the histogram, the moments are obtained as

$$\mu_n = \frac{\sum [f(x_i) - \mu]^n}{\sum f(x_i)} \quad (23)$$

where, $f(x)$ is the bin-count data of the histogram and n indicates the order of the moment about the mean, μ . A synthetic time series is generated at the inflow boundary using a standard first order moving average, with the help of 2nd and 4th moments [45]. Hence, we have

$$x_t = e_t + \alpha_{fst} e_{t-1} \quad (24)$$

where, e_t is defined by a Gaussian distribution which has zero first moment and standard deviation defined as σ . Since Gaussian distribution is symmetric, every odd central moment is zero and the first two even central moments are defined as

$$\mu_2(e_t) = \sigma^2 \quad (25)$$

$$\mu_4(e_t) = 3\sigma^4 \quad (26)$$

Since at every t , e_t and e_{t-1} are uncorrelated, the 2nd and 4th central moments of the moving average model can be

described as

$$\mu_2(x_t) = \sigma^2(1 + \alpha_{fst}^2) \quad (27)$$

$$\mu_4(x_t) = \sigma^4(1 + \alpha_{fst}^4) \quad (28)$$

These two moments are compared with the moment values obtained from the histogram and the most suitable values of σ and α_{fst} are obtained by the method of grid search, such that the difference between the moments of synthetic disturbance generated and that available experimentally is kept minimum, of the order of 10^{-7} . In addition to the moving average part, the model is modified to consider the low frequency data of FST, based on experimental results [48]. This is important since the large-scale anisotropy of the incoming flow is retained for a low frequency range. Thus, the net stream wise disturbance component becomes

$$u' = e_t + \alpha_{fst} e_{t-1} + \sum_{j=1}^N a_j e^{ik_j(x - c_{ph}t)} \quad (29)$$

where first two terms are given by the Gaussian distribution and the last term is due to the low frequency components of the disturbance which is facility and speed dependent; c_{ph} being the phase speed of propagation of these low wavenumber coherent structures. The Gaussian distribution is obtained from uniformly distributed random numbers,

which is converted to normal distribution using box-Muller method. We use the obtained values of σ and α_{fst} in Eq. (29), whereas the low wavenumber disturbance is obtained from the experimental velocity distribution directly. Figure 2 shows experimentally obtained empty tunnel disturbance data along with the reconstructed signal from Eq. (29). The bottom frame shows FFT of the same.

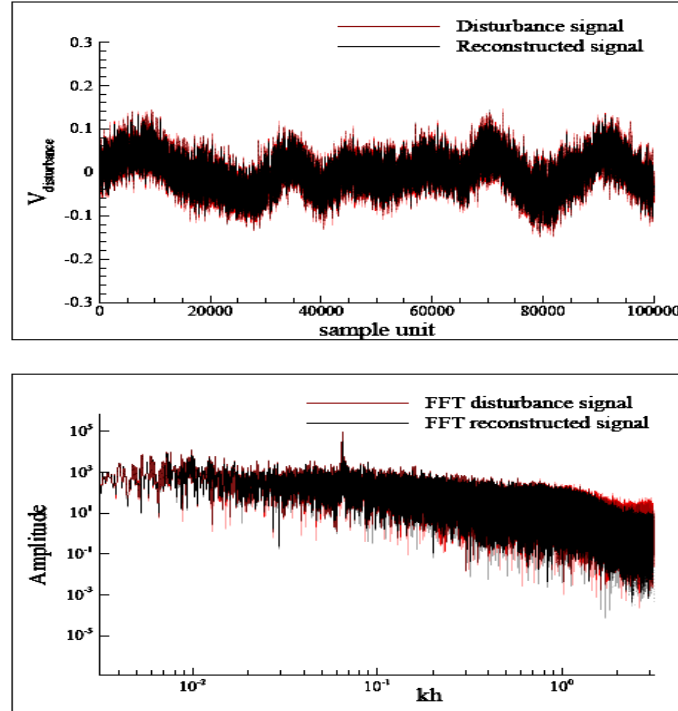


FIG. 2 COMPARISON OF EXPERIMENTAL DISTURBANCE SIGNAL AND RECONSTRUCTED DISTURBANCE SIGNAL (TOP) USING MOVING AVERAGE METHOD OF FST MODEL AND FFT OF THE SAME (BOTTOM).

Results and Discussion

Here, we have considered cases of $Re = 60,000$ and $400,000$ and simulations are done with and without FST. DNS of flow past AG24 airfoil is done in the range of angles of attack, $-6^\circ \leq \alpha \leq +6^\circ$. The AG24 airfoil is a thin airfoil developed [2], basically for RC model. Similar low Re sections can be used for MAV applications. This airfoil has a

thickness of 8.4% and camber of 2.2%, with the lower surface flatness is 72.2% and the leading edge radius is 0.6%.

Table 1 shows the different cases studied in this work.

TABLE 1 DIFFERENT CASES STUDIED IN PRESENT WORK

Case	Reynolds number	FST
1	60,000	No FST
2	60,000	0.18%
3	400,000	No FST
4	400,000	0.18%

Case 1: $Re = 60000$ without FST

Figure 3 shows streamline and vorticity contours for the indicated angles of attack at instantaneous time of 50 and Figure 4 shows the time-averaged C_p plots for $Re = 60,000$ at the considered α values, for $0 \leq t \leq 50$.

The variations on top and bottom surfaces indicate existence of adverse pressure gradient due to recirculating bubbles. It is seen that the mean pressure on top surface has higher positive values, than that is on the bottom surface for higher positive α 's.

Figure 5 shows the time-averaged lift curve and drag polar for $Re = 60,000$ for without FST case. Here time averaging is performed by taking data from $t=0$ to 50.

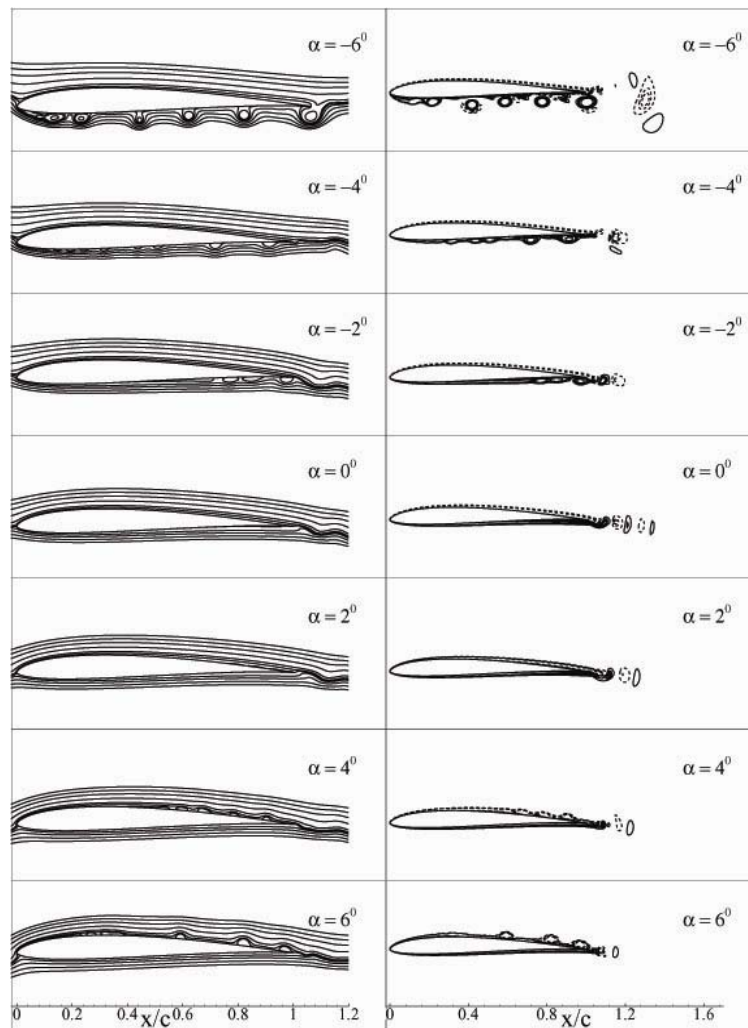


FIG. 3 STREAMLINE (LEFT) AND VORTICITY (RIGHT) CONTOURS OF AG24 AIRFOIL AT INDICATED ANGLES OF ATTACK WITHOUT FST AT $Re = 60000$ AND $t = 50$.

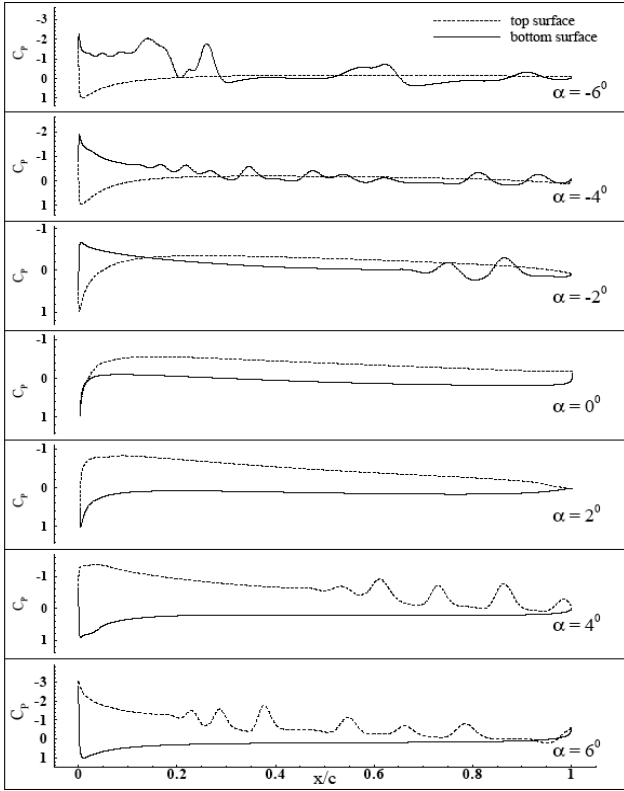


FIG. 4 TIME-AVERAGED C_p PLOTS FOR $Re = 60,000$ AT CONSIDERED α VALUES WITHOUT FST.

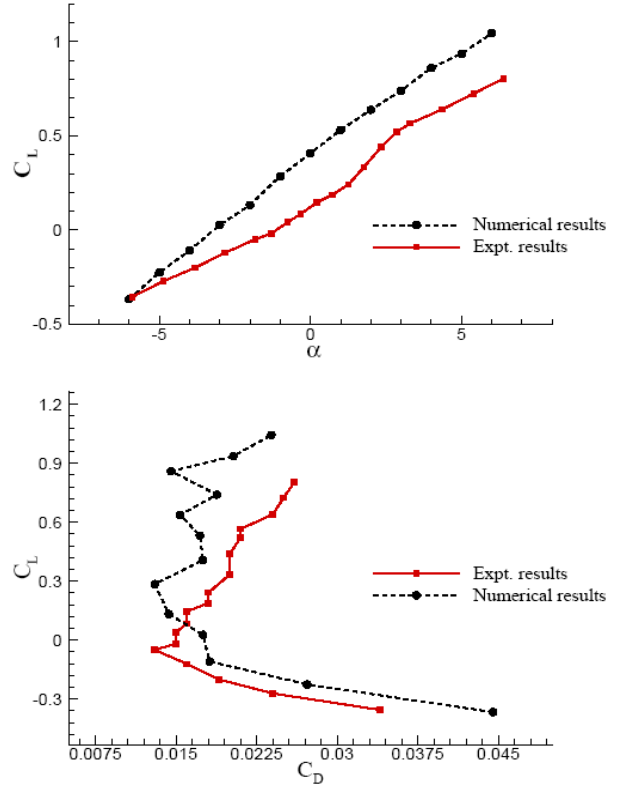


FIG. 5 LIFT CURVE (TIME-AVERAGED LIFT) AND DRAG POLAR FOR $Re = 60,000$, WITHOUT FST.

The numerical results obtained here are compared with the experimental data [2], which shows fair qualitative agreement. As the computations are performed without FST, computed lift values are predictably higher at all angles of attack. The expected improvement by incorporating FST is shown later for the higher Re case. It is also seen that the numerically obtained C_D is slightly over-predicted by the computational results, for higher negative values of α and under-predicted for higher positive values of α .

Case 2: Flow with Turbulence Intensity of 0.18% ($Re=60000$)

Here, DNS of flow past the AG24 airfoil is performed in the presence of FST for $Re = 60,000$, in the range of angles of attack $-6^\circ \leq \alpha \leq +6^\circ$, with the turbulence intensity of 0.18%. Figure 6 shows streamline and vorticity contours for the indicated angles of attack at instantaneous time, $t = 50$ with the flow patterns showing the effects of FST.

Unlike the previous case without FST, where vortex shedding is predominantly along the mean line, here there is elongated shedding, which becomes more intense with increase in α . It is also seen that for higher positive α , weaker positive vortices are created, aided by secondary instabilities on the top surface. Furthermore, it is seen from the streamline contours for lower negative α flow reversal is noted at the trailing edge.

Figure 7 shows the time-averaged C_p plot for the indicated α for $0 \leq t \leq 50$. Observed variations on top and bottom surfaces are proportional to the intensity of adverse pressure gradient. It can be seen that the positive α provides greater lift with FST, which is correspondingly more negative for the negative α 's.

Figure 8 shows the time-averaged lift curve and drag polar for the case with FST, for $Re = 60,000$ in the time range $0 \leq t \leq 50$. Numerical results obtained are compared with the experimentally available data [2], though exact information on FST is not available for the experimental facility. Hence we have considered a very low level of turbulence intensity for the computed case.

It can be seen that the lift curve shows a greater match with the experimental data available, than the previous case without FST. Similarly for the drag polar also, it can be noted that the deviation from experimental results has decreased compared to no FST case.

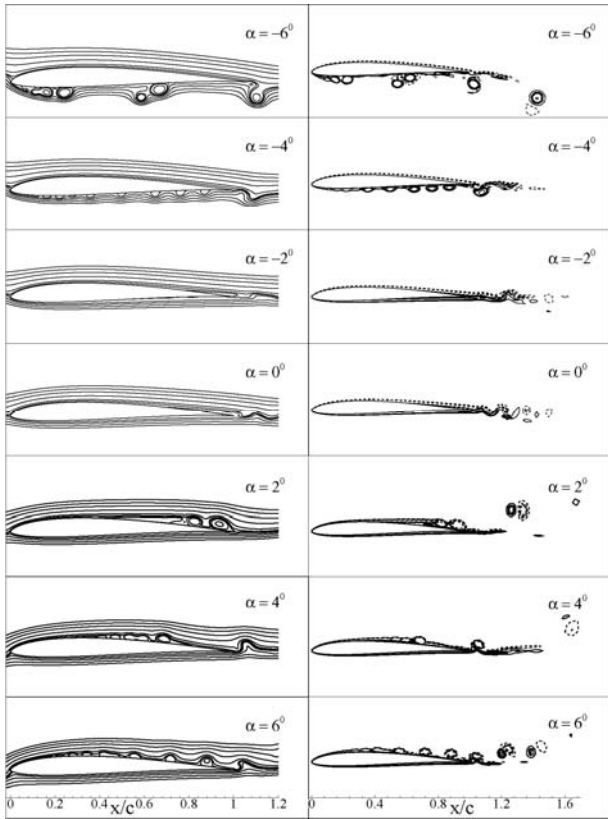


FIG. 6 STREAMLINE (LEFT) AND VORTICITY (RIGHT) CONTOURS AT INDICATED ANGLES OF ATTACK WITH 0.18% FST AT $Re = 60000$ AND $t = 50$.

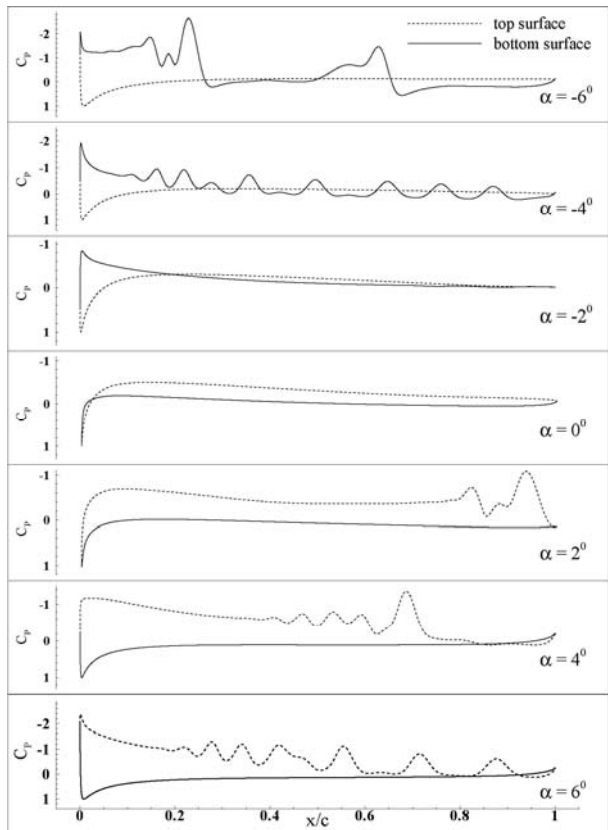


FIG. 7 TIME-AVERAGED C_p PLOTS AT THE CONSIDERED α VALUES FOR CASE-2.

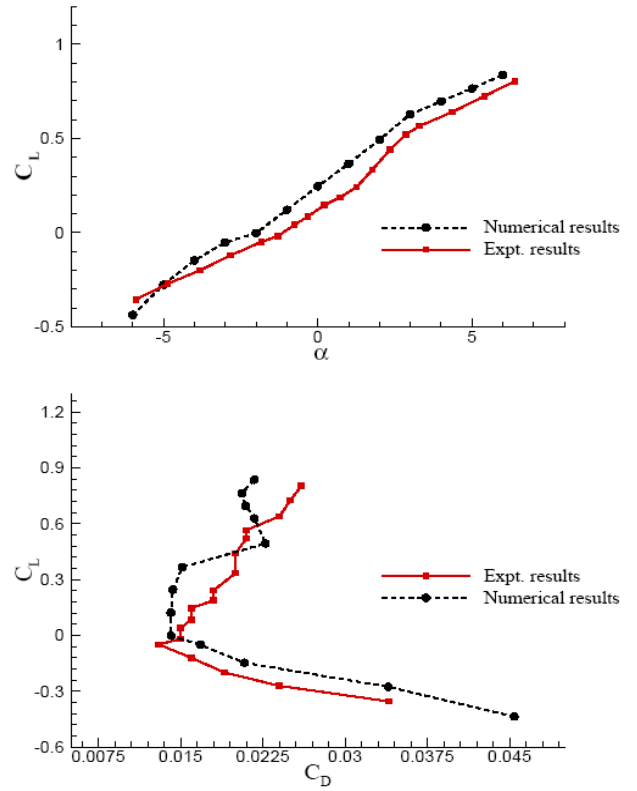


FIG. 8 LIFT CURVE AND DRAG POLAR FOR $Re=60000$ WITH 0.18% FST.

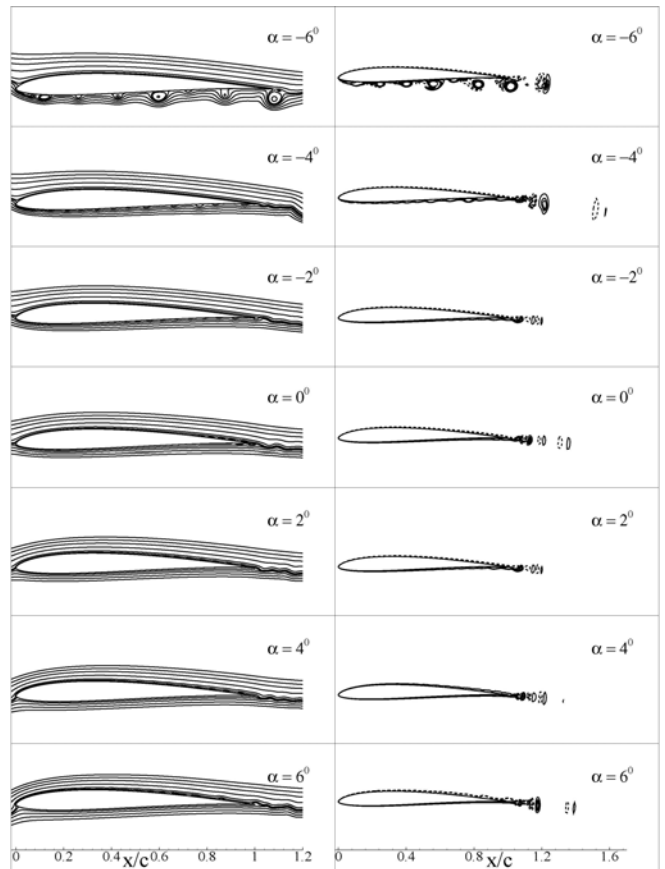


FIG. 9 STREAMLINE (LEFT) AND VORTICITY (RIGHT) CONTOURS AT INDICATED ANGLES OF ATTACK WITHOUT FST AT $Re = 400000$ AND $t = 30$.

Case 3: $Re = 400,000$ without FST

Next the sensitive dependence of flow on FST with low Re is studied, by considering another case of higher Reynolds number, $Re = 400,000$ - in the range of angles of attack from -6° to 6° . Consolidated numerical results are presented here in the form of lift-curve and drag-polar, which are compared with the experimental results [2].

Figure 9 shows instantaneous streamline and vorticity contours at $t = 30$ for the indicated α for $Re = 400,000$. It is seen that major vortices are shed along the mean line. Also, the shedding pattern is such that these are alternating in sign. Negative sign vortices are shown in dotted lines.

Figure 10 shows the time-averaged C_p plots for $Re = 400,000$ at the indicated angles of attack for $0 \leq t \leq 50$, which explains corresponding separation phenomenon and lift coefficient; the fluctuations in the plot corresponding to the zones of separation and reattachment.

Figure 11 shows the lift curve and drag polar for the flow $Re = 400,000$ using time-averaged lift and drag coefficients for the considered α for $0 \leq t \leq 50$. Numerical results obtained are compared with the experimental results available in [2]. It can be seen that the numerically obtained C_D is slightly over-predicted in the computations, for negative α . The difference between numerically obtained value and the experimentally available results can be attributed to the effects of free stream turbulence, which is present inherently in every experimental setup. An accurate modelling of FST proves to be indispensable in solving the full NS equation and subsequent flow predictions at low Re .

Case 4: Flow past AG24 airfoil with 0.18% FST ($Re = 400,000$)

Next, we consider the effects of FST for the higher Re case. In the absence of exact FST level for this case, we once again take a nominal value of turbulence intensity of 0.18% for this case also.

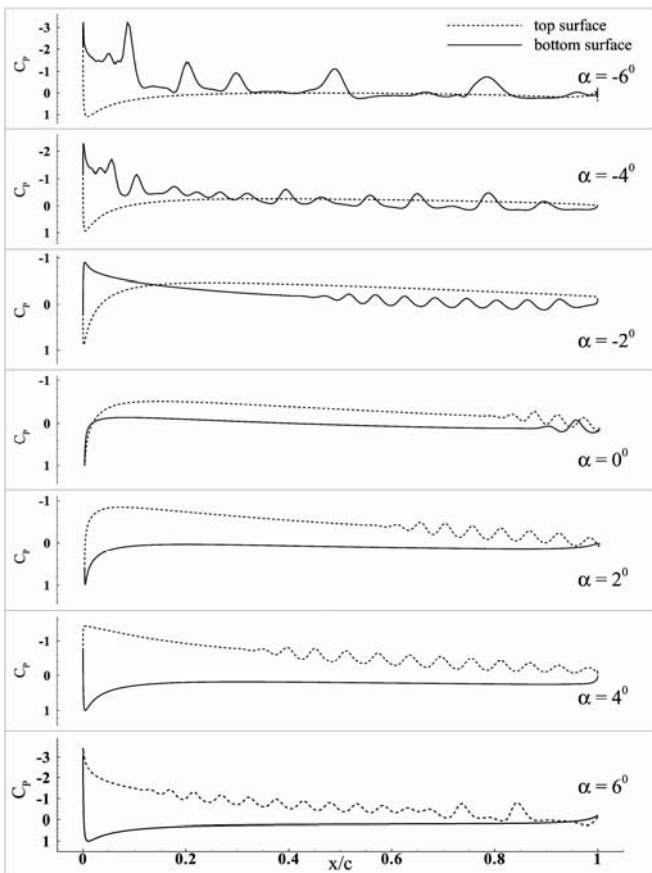


FIG. 10 TIME-AVERAGED C_p PLOTS AT INDICATED ANGLES OF ATTACK WITHOUT FST AND $Re = 400000$

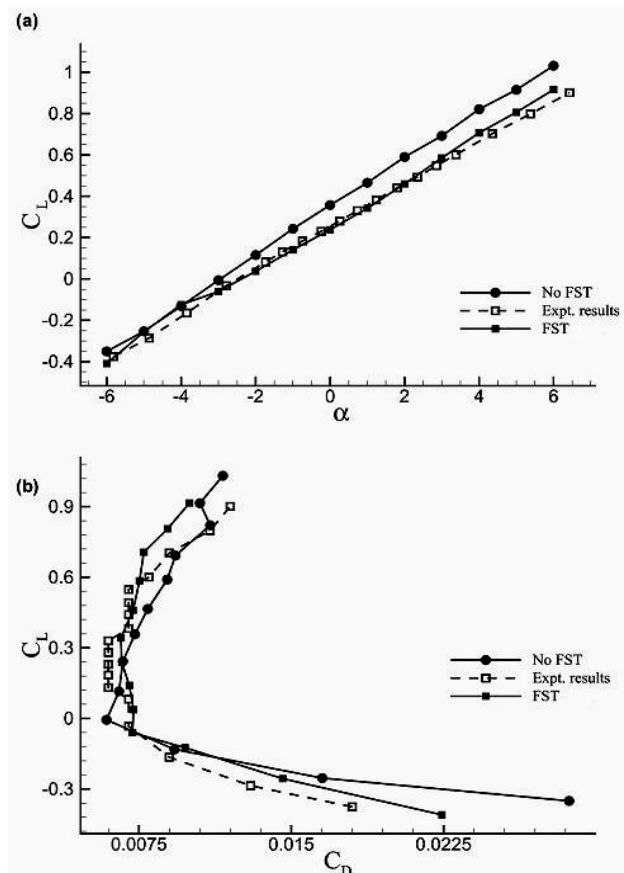


FIG. 11 COMPARISON OF EXPERIMENTAL [2] AND NUMERICAL RESULTS ARE FOR WITH AND WITHOUT FST: a) LIFT CURVE, b) DRAG POLAR

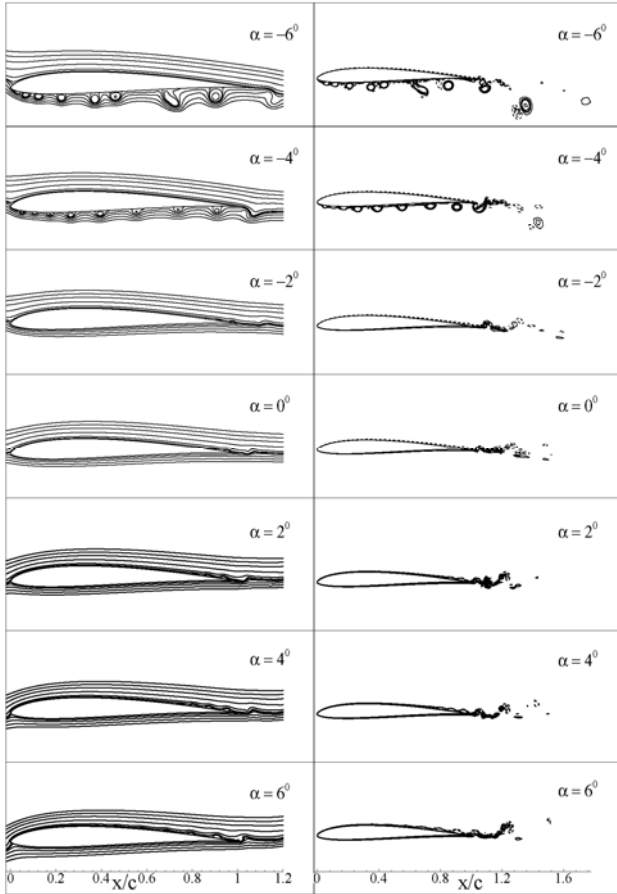


FIG. 12 STREAMLINE (LEFT) AND VORTICITY (RIGHT) CONTOURS AT INDICATED ANGLES OF ATTACK WITH 0.18% FST FOR $Re = 400000$ AND AT $t=30$.

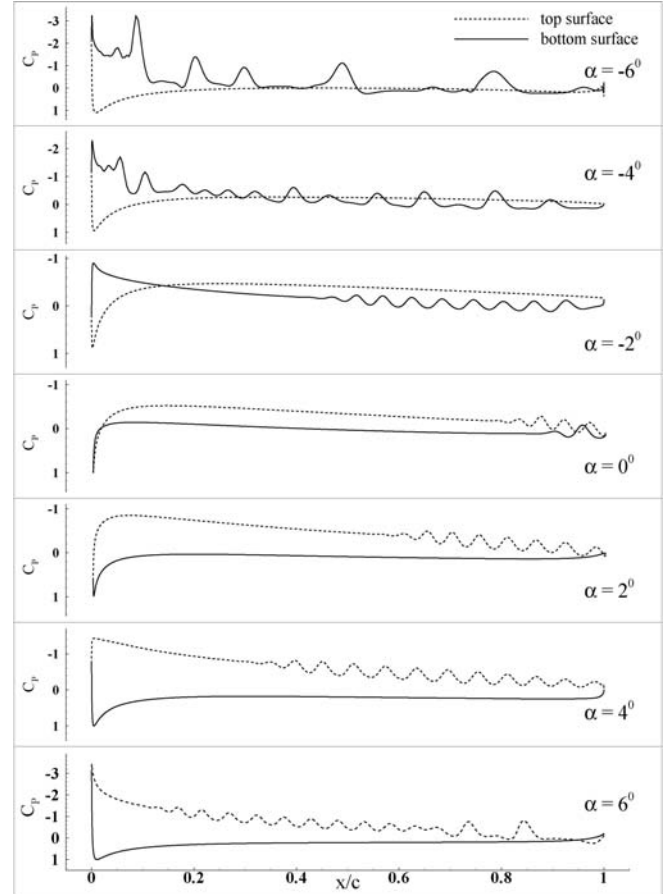


FIG. 13 TIME-AVERAGED C_p PLOTS AT MENTIONED ANGLES OF ATTACK AND $Re = 400,000$ WITH 0.18% FST.

Figure 12 shows the streamline and vorticity contours of AG24 airfoil at indicated α with 0.18% FST for $Re = 400000$ at $t = 30$, while figure 13 shows the time-averaged C_p plots at the indicated α for $0 \leq t \leq 50$. Observed variations indicate flow separation and reattachment phenomena and the intensity of adverse pressure gradient. From Fig. 11 the lift curve and drag polar for $Re = 400,000$ with and without FST can be compared with the experimental results [2]. It is seen that the lift curve almost coincides with the experimental value with FST. Drag polar also shows a greater degree of match with the experimental data, as compared to the results without FST. Effects of FST show marked deviation in vortex shedding, which now happens in pair, unlike the cases without FST, where vortex shedding occurs alternating in sign. Also the shedding which previously happened along the mean line, now undergo greater variations. With FST, we see a dominant shedding at an angle to the mean line and a minor elongated shedding along the mean line. A flow influenced by FST is a case where disturbance is externally forced.

Conclusions

Analysis of low Re flows and their sensitivity to background FST is performed here by DNS of flow past AG24 airfoil. FST is modelled stochastically using the moving average method. It is seen that there is clear presence of laminar separation bubbles because of the low Re associated. The flow is greatly influenced by these bubbles, with points/zones of separation and reattachment witnessing larger variation in pressure as seen in C_p plots.

Effect of Angle of Attack

Influence of α can be directly noted from streamline and vorticity contours. With increasing α extent of separation bubble, associated non-linear lift increases along with the increase in pressure drag that can be attributed to the increase in effective thickness due to the separation bubbles. For the AG24 airfoil at positive α , on the top surface

separation bubble is stronger. This is owing to greater adverse pressure gradient after initial flow acceleration and variations in pressure and velocity are more rapid. However, for negative α , there is no initial acceleration, with less intense adverse pressure gradient, resulting in weaker separation bubbles.

Effects of Reynolds Number and FST

The effects of Re is clearly evident due to lower sensitivity to FST at higher value of Re . This delays the formation of separation bubbles, as well as, reduces their extent. Also the upstream propagation of bubbles, which happens due to high adverse pressure gradient is also reduced with increase in Re . Introduction of FST shows marked deviation in the vortex shedding pattern, which happens in pair, unlike the case of without FST, where vortex shedding occurs alternate in sign. A flow influenced by FST is a case where disturbance is externally forced. Hence the mode of transition also changes. The effects of α , camber and Re remains qualitatively same in the presence of FST.

The omnipresent nature of FST becomes very evident from the comparison of the time averaged lift curve and drag polar of the considered cases with experimental results. Though the exact FST in the experimental facility is unknown, it is noted that the computational results show a very good match, with the experimental results. Thus, it becomes moot that in realistic comparison with experimental data for low Re one must incorporate FST effects through a physical model, as it has been reported here. This is a very important finding.

ACKNOWLEDGEMENT

The authors acknowledge the support of NPMICAV program, India for supporting this research.

REFERENCES

- [1] T. K. Sengupta, High Accuracy Computing Methods, Cambridge University Press, New York, 2013.
- [2] G. A. Williamson, B. D. McGranahan, B. A. Broughton, R. W. Deters, J. B. Brandt, M. S. Selig, Summary of Low Speed Airfoil Data, volume 5, Dept. of Aerospace Engineering, University of Illinois at Urbana-Champaign, 2007.
- [3] S. Ho, H. Nassef, N. Pornsinsirak, Y. C. Yai, C. M. Ho, Unsteady aerodynamics and flow control for flapping wing flyers, Prog. Aerospace Sci. 39 (2003) 635–681.
- [4] T. K. Sengupta, V. Vikas, A. Johri, An improved method for calculating flow past flapping and hovering airfoils, Theo. and Comput. Fluid Dyn. 19(6) (2006) 417–440.
- [5] P. Freymuth, Thrust generation by an airfoil in hover mode, Expts. Fluids 9 (1990) 17–24.
- [6] D. J. Pines, F. Bohorquez, Challenges facing future micro-air-vehicle development, J. aircraft 23(2) (2006) 315–356.
- [7] G. E. Torres, T. J. Mueller, Aerodynamics of low aspect ratio wings at low Reynolds numbers with applications to micro air vehicle design, Report for Naval Research Laboratory (2001).
- [8] T. J. Mueller, Aerodynamic measurements at low Reynolds numbers for fixed wing micro-air vehicles, Proceedings of the Development and Operation of UAVs for Military and Civil Applications Short Course (2000).
- [9] T. J. Mueller, L. J. Pohlen, P. E. Conigliaro, B. J. H. Jr., The influence of free-stream disturbances on low Reynolds number airfoil experiments, Experiments in Fluids. 1 (1983) 3–14.
- [10] L. J. Pohlen, Experimental studies of the effect of boundary layer transition on the performance of the miley (m06-13-128) airfoil at low Reynolds numbers, Master's Thesis, The University of Notre Dame (1983).
- [11] S. J. Miley, An analysis of the design of airfoil sections for low Reynolds numbers, Ph.D. Dissertation, Mississippi State University (1972).
- [12] M. Gaster, The structure and behavior of separation bubbles, Aerodynamics Division N.P.L. Reports and Memoranda No. 3595 (1967).
- [13] T. J. Mueller, L. J. Pohlen, P. E. Conigliaro, B. J. H. Jr., Blade row interactions, transition and high-lift aerofoils in low-pressure turbines, Annu. Rev. Fluid Mech. 37 (2005) 71–98.
- [14] L. L. Pauley, P. Moin, W. C. Reynolds, The structure of two-dimensional separation, J. Fluid Mech. 220 (1990) 397–411.

- [15] S. Burgmann, J. Dannemann, W. Schroder, Time-resolved and volumetric PIV measurements of a transitional separation bubble on an sd7003 airfoil, *Exp. Fluids*. 44 (2008) 602–622.
- [16] C. Sicot, S. Aubrun, S. Loyer, P. Devinant, Unsteady characteristics of the static stall of an airfoil subjected to free stream turbulence level up to 16%, *Exp. Fluids*. 41 (2006) 641–648.
- [17] W. H. Melbourne, Turbulence and the leading edge phenomenon, *J. Wind Engineering and Industrial Aerodynamics* 49 (1993) 45–64.
- [18] W. B. Roberts, Calculation of laminar separation bubbles and their effect on airfoil performance, *AIAA Journal* 18(1) (1980) 25–31.
- [19] J. Stack, Tests in the variable density wind tunnel to investigate the effects of scale and turbulence on airfoil characteristics, NACA-TN-364, NACA Langley Memorial Aeronautical Laboratory (1931).
- [20] E. D. Jancauskas, The cross-wind excitation of bluff structures and the incident turbulence mechanism, Doctoral thesis, Monash University, Clayton (1983).
- [21] P. Devinant, T. Laverne, J. Hureau, Experimental study of wind-turbine airfoil aerodynamics in high turbulence, *J. Wind Engineering and Industrial Aerodynamics* 90 (2002) 689–707.
- [22] K. Swalwell, The effect of turbulence on stall of horizontal axis wind turbines, PhD Thesis, Department of Mechanical Engineering, Monash University (2005).
- [23] Q. S. Li, W. H. Melbourne, The effect of large-scale turbulence on pressure fluctuations in separated and reattaching flows, *J. Wind Engineering and Industrial Aerodynamics* 83 (1999) 159–169.
- [24] P. J. Saathoff, Effects of free-stream turbulence on surface pressure fluctuations in separated and reattaching flows, Ph.D. Thesis, Monash University (1988).
- [25] R. Hillier, N. J. Cherry, The effects of stream turbulence on separation bubbles, *J. Wind Engineering and Industrial Aerodynamics* 8 (1981) 49–58.
- [26] E. Cruz, S. Watkins, B. Loxton, A study of the effects of turbulence on airfoils at low Reynolds numbers, Interim Report AOARD-06-4037, Melbourne: RMIT University (2007).
- [27] B. Loxton, S. Watkins, J. Watmuff, P. Trivalio, E. Cruz, S. Ravi, The influence of atmospheric turbulence on the aerodynamics of a flat plate micro air vehicle wing, 3rd Australasian Unmanned Air Vehicles Conference. Melbourne, Australia (2009).
- [28] J. Watmuff, Evolution of a wave packet into vortex loops in a laminar separation bubble, *J. Fluid Mech.* 397 (1999) 119–169.
- [29] T. K. Sengupta, *Fundamentals of Computational Fluid Dynamics*, University Press, Hyderabad, 2004.
- [30] P. G. Esposito, R. Verzicco, P. Orlandi, Boundary condition influence on the flow around a circular cylinder, In the proceedings of IUTAM Symposium on Bluff-Body Wakes, Dynamics and Instabilities, Springer-Verlag, Berlin, Germany, 47-50 (1993).
- [31] C. S. Chew, K. S. Yeo, C. Shu, A generalized finite-difference (GFD) ALE scheme for incompressible flows around moving solid bodies on hybrid mesh-free Cartesian grids, *J. Comput. Phys.* 218 (2006) 510–548.
- [32] H. Ding, C. Shu, K. S. Yeo, D. Xu, Numerical simulation of flows around two circular cylinders by mesh-free least square-based finite difference methods, *Int. J. Numer. Meth. Fluids* 53 (2007) 305–332.
- [33] M. T. Nair, T. K. Sengupta, Orthogonal grid generation for Navier-Stokes computations, *Int. J. Num. Meth. Fluids* 28 (1998) 215–224.
- [34] G. Ryskin, L. G. Leal, Orthogonal mapping, *J. Comput. Phys.* 50 (1983) 71–100.
- [35] R. Duraiswami, A. Prosperetti, Orthogonal mapping in two dimensions, *J. Comput. Phys.* 98 (1992) 254–268.
- [36] L. Eca, 2D orthogonal grid generation with boundary point distribution control, *J. Comput. Phys.* 125 (1996) 440–453.
- [37] T. K. Sengupta, G. Ganerwal, S. De, Analysis of central and upwind compact schemes, *J. Comput. Phys.* 192 (2003) 677–694.

- [38] M. K. Rajpoot, T. K. Sengupta, P. K. Dutt, Optimal time advancing dispersion relation preserving schemes, *J. Comput. Phys.* 229 (2010) 3623–3651.
- [39] H. A. V. der Vorst, Bi-CGSTAB: A fast and smoothly converging variant of Bi-CG for the solution of non-symmetric linear systems, *SIAM J. Sci. Stat. Comput.* 13(2) (1992) 631–644.
- [40] T. K. Sengupta, M. K. Rajpoot, Y. G. Bhumkar, Space-time discretizing optimal DRP schemes for flow and wave propagation problems, *Comput. Fluids* 47 (2011) 144–154.
- [41] T. K. Sengupta, Y. Bhumkar, V. Lakshmanan, Design and analysis of a new filter for LES and DES, *Comput. Struct.* 87 (2009) 735–750.
- [42] T. K. Sengupta, Y. G. Bhumkar, New explicit two-dimensional higher order filters, *Comput. Fluids* 39 (2010) 1848–1863.
- [43] Y. G. Bhumkar, T. K. Sengupta, Adaptive multi-dimensional filters, *Comput. Fluids* 49 (2011).
- [44] T. K. Sengupta, S. De, K. Gupta, Effect of free-stream turbulence on flow over airfoil at high incidence, *J. Fluids Struct.* 15 (2001) 671–690.
- [45] W. A. Fuller, *Introduction to Statistical Time Series*, Cambridge Univ. Press, Cambridge, UK, 1995.
- [46] D. Lucor, G. E. Karniadakis, Noisy inflows cause a shedding mode switching in flow past an oscillating cylinder., *Phys. Rev. Letters* 92 (2004) 154501–1–154501–4.
- [47] U. Frisch, *Turbulence*, Wiley, New York, 1978.
- [48] T. K. Sengupta, D. Das, P. Mohanamurthy, V. K. Suman, A. Biswas, Modeling free-stream turbulence based on wind tunnel and flight data for instability studies, *Emerging Multidisciplinary Fluid Sciences* 1(3) (2009).
- [49] Tapan K. Sengupta, Yogesh G. Bhumkar, Direct numerical simulation of transitional flow over a NLF airfoil: Methods and validation, *Frontiers in Aerospace Engineering*, 2(1), (2013), 39-52.



Prof. Tapan K. Sengupta is professor in department of Aerospace Engineering at Indian Institute of Technology Kanpur, India. He has done his Ph.D. from Georgia Tech. University and has been involved in research and teaching CFD for more than two decades in India and abroad. His interests include developing CFD techniques for high accuracy computing of transitional and turbulent flows and high resolution schemes for compressible flows and problems of atmospheric sciences. Theoretical fluid mechanics continues to be his area of primary interest. He established High Performance Computing Laboratory at the Aerospace Engineering Department of I.I.T. Kanpur which has been an active place of research right from its inception in 1990. The emphasis of research is on developing high accuracy computing methods to aid in bridging the gap between theoretical and computational fluid dynamics and heat transfer. He is actively involved in the research areas like transition and turbulence, unsteady aerodynamics, bluff body flows, flow control, scientific computing and high accuracy numerical methods. Prof. Sengupta is corresponding author of the paper who can be contacted at tksen@iitk.ac.in and more details regarding ongoing research can be found out on <http://spectral.iitk.ac.in>.

The Velocity Increment for Hohmann Coplanar Transfer from Different Low Earth Orbits

Shkelzen Cakaj^{*1}, Bexhet Kamo², Algenti Lala³, Elson Agastra⁴, Ilir Shinko⁵

Faculty of Information Technology, Polytechnic University of Tirana, Albania

^{*1}shkelzen.cakaj@fulbrightmail.org; ²bkamo@fti.edu.al; ³alala@fti.edu.al; ⁴eagastra@fti.edu.al;

⁵ishinko@fti.edu.al

Abstract

The transfer of satellites in too high orbits as geosynchronous one (geostationary), usually is achieved firstly by launching the satellite in Low Earth Orbit (LEO), then in elliptical transfer orbit and finally to the geosynchronous orbit. The three steps process is known as Hohmann transfer. The Hohmann transfer which involves two circular orbits with different orbital inclinations is known as non-coplanar Hohmann transfer. If both orbital planes are aligned the Hohmann transfer is known as coplanar what is further considered in this paper. In terms of propellant consumptions the Hohmann transfer is the best known transfer to be applied when transferring between circular coplanar orbits. For transfer between circular coplanar orbits, the given information usually consists of the radii of the initial and final orbits. The velocity to be applied into two orbit points in order to attain the dedicated final orbit is analyzed. The aim of this paper is to conclude about the velocity changes under the different initial low Earth altitudes. For different initial orbit altitudes, the velocities to be applied in process of Hohmann transfer are simulated. From respective simulations, the velocity variations on dependence of initial altitudes are derived. The eccentricity is considered, too.

Keywords

LEO; Satellite; Orbit; Hohmann Transfer

Introduction

When launching and then consolidating the satellite on its own high circular orbit (ex. geosynchronous), the needed satellite's propellant mass must be minimized. The Hohmann transfer is well known for the minimum of propellant mass used for satellite transfer into high orbits.

The Hohmann transfer is the best transfer to be used when transferring between circular coplanar orbits [1]. For transfer between circular coplanar orbits, the information usually given consists of the radii of the initial and final orbits. Due to the reversibility of orbits, Hohmann transfer orbits also work to bring a spacecraft from the higher orbit into the lower one. The Hohmann transfer orbit is based on two instantaneous velocity changes. The transfer consists of a velocity impulse on an initial circular orbit, in the direction of motion and collinear with velocity vector, which propels the space vehicle into an elliptical transfer orbit. The second velocity impulse also in the direction of motion is applied at apogee of the transfer orbit which propels the space vehicle into a final circular orbit at the final altitude [1, 2].

This paper is motivated by the fact that the problem of Hohmann transfer by [3] is analyzed with three normalized radii, and our approach is based on the single normalized radius for the coplanar transfer case. The non coplanar transfer involves also allocating the total plane change angle between two maneuvers [2].

Under the first section the elliptic orbit is generally considered. Further, through implementation of the single normalized radius, both velocity impulses to be applied at perigee and apogee of the Hohmann transfer orbit are analyzed. Considering different initial low Earth orbit altitudes respective velocities are calculated. Finally, these results are discussed and closed by conclusions.

Elliptic Orbit

The path of the satellite's motion is an orbit. Generally, the orbits of communication satellites are ellipses laid on the orbital plane defined by *space orbital parameters*. These parameters (Kepler elements) determine the position of the orbital plane in space, the location of the orbit within orbital plane and finally the position of the satellite in the appropriate orbit [4,5]. The exactly know position of the satellite in space enables the communication between the satellite and ground stations (users) [6]. For reliable communication, during the link budget calculations atmospheric impairments and interference aspects have carefully to be considered [7, 8]. The communication between the satellite and a ground station is established only when the satellite is stabilized in its own orbit. Thus, permanent attitude control is mandatory. In terms of attitude control performance the satellite reaction wheel's configuration also plays an important role in providing the attitude control torques [9]. Different algorithms are applied and active control means are generally added to assure accurate attitude stabilization, keeping the attitude errors within permitted limits, consequently keeping the reliable communication [10, 11].

The elliptic orbit is determined by the semi-major axis which defines the size of an orbit, and the eccentricity which defines the orbit's shape. Orbits with no eccentricity are known as circular orbits. The elliptic orbit shaped as an ellipse, with a maximum extension from the Earth center at the apogee (r_a) and the minimum at the perigee (r_p) is presented in Figure 1.

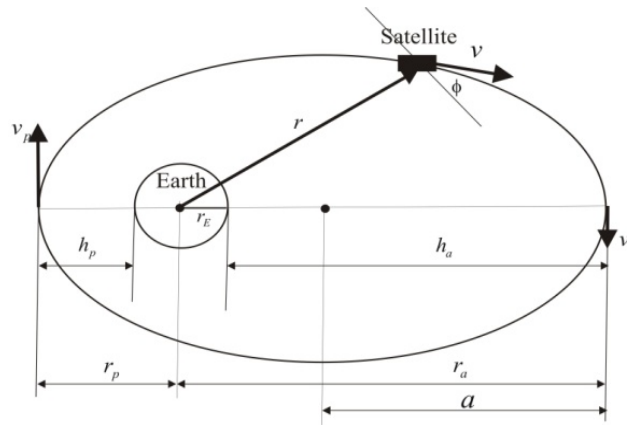


FIGURE 1. MAJOR PARAMETERS OF AN ELLIPTIC ORBIT.

The orbit's eccentricity is defined as the ratio of difference to sum of apogee (r_a) and perigee (r_p) radii as, [4]-[5].

$$e = \frac{r_a - r_p}{r_a + r_p} \quad (1)$$

Applying geometrical features of ellipse yield out the relations between semi major axis, apogee and perigee:

$$r_p = a(1 - e) \quad (2)$$

$$r_a = a(1 + e) \quad (3)$$

$$2a = r_a + r_p \quad (4)$$

both, r_p and r_a are considered from the Earth's center. Earth's radius is $r_E = 6378$ km. Then, the altitudes (highs) of perigee and apogee are:

$$h_p = r_p - r_E \quad (5)$$

$$h_a = r_a - r_E \quad (6)$$

Different methods are applied for satellite injection missions. Goal of these methods is to manage and control the satellite to safely reach the low Earth orbit, and then to the transfer elliptical orbit and finally the geosynchronous orbit [12]-[14]. The Hohmann transfer is considered as the most convenient.

The specific orbit implementation depends on satellite's injection velocity. The orbit implementation process on the

best way is described in terms of the cosmic velocities. Based on Kepler's laws, considering an elliptic orbit, the satellite's velocity at the perigee and apogee point, respectively are expressed as [4, 5],

$$v_p = \sqrt{\left(\frac{2\mu}{r_p}\right) - \left(\frac{2\mu}{r_a + r_p}\right)} \quad (7)$$

$$v_a = \sqrt{\left(\frac{2\mu}{r_a}\right) - \left(\frac{2\mu}{r_a + r_p}\right)} \quad (8)$$

$$v_p \cdot r_p = v_a \cdot r_a = vrcos\Phi \quad (9)$$

$\mu = m \cdot G = 3.986 \cdot 10^5 km^3 / s^2$, G is the Earth's gravitational constant and m is Earth's mass, Φ represents an angle between a satellite vector \mathbf{r} and local horizon at satellite point. For orbit with no eccentricity ($e = 0$), apogee and perigee distances are equal ($r_a = r_p = r$), thus orbit becomes circular with radius r and orbital velocity as [2]:

$$v_1 = \sqrt{\frac{\mu}{r}} \quad (10)$$

By definition this is called the *first cosmic velocity*, enabling the satellite to orbit circularly around the Earth at the uniform velocity according to (10). If the injection velocity happens to be less than the first cosmic velocity, the satellite follows a ballistic trajectory and falls back to the Earth [4, 5]. The *second cosmic velocity* is expressed as,

$$v_2 = \sqrt{\frac{2\mu}{r}} \quad (11)$$

A spacecraft under second cosmic velocity leaves the Earth's gravity. For injection velocity v_p at perigee more than the first cosmic velocity and less than the second cosmic velocity the orbit is elliptical with an eccentricity in between 0 and 1. This is expressed as:

$$v_1 < v < v_2 \quad (12)$$

$$0 < e < 1 \quad (13)$$

The satellite injection point is at perigee, and the apogee distance attained in the elliptical orbit depends upon the injection velocity. The higher is the injection velocity at perigee, the greater is the apogee distance. For the same perigee distance r_p , if under the injection velocity v_{p1} at perigee it is attained an apogee distance r_{a1} , and under velocity v_{p2} it is attained an apogee distance r_{a2} , then applying (7) yields out the relationship between velocities at perigee and respective attained distances at apogee.

$$\left(\frac{v_{p2}}{v_{p1}}\right)^2 = \frac{1 + \frac{r_p}{r_{a1}}}{1 + \frac{r_p}{r_{a2}}} \quad (14)$$

Coplanar Hohmann Transfer

The Hohmann coplanar transfer orbit is an elliptic orbit used to transfer between two circular orbits of different radii in the same plane. The first (low radius) circular orbit is defined as *initial* and the second (high radius) is defined as a *final orbit*. The orbital maneuver to perform the Hohmann transfer applies two engine impulses (thrusts), one to move a space craft onto the transfer orbit and a second to move off it. For the coplanar Hohmann transfer, two applied velocity impulses are confined to the orbital planes of the initial and final orbits.

The transfer from the low radius orbit to the high radius orbit is attained in three steps. The first one is the launch of the satellite in the low Earth circular orbit (LEO). This is the *initial* circular orbit with radius of r_i as it is presented in Figure 2. By the second step, the first velocity impulse (Δv_1) is applied at the low Earth orbit creating an elliptic transfer orbit with perigee altitude equal of the initial circular orbit and the apogee altitude equal to the

final circular orbit. Finally, at the third step, the second velocity impulse (Δv_2) is applied at apogee of the transfer orbit in order to attain the final orbit, respectively the geosynchronous circular orbit (GEO) with radius (r_f) as presented in Figure 2. The apogee of the transfer orbit is equal to the radius of the final orbit. Thus, the second velocity impulse circularizes the transfer orbit at apogee. Both velocity impulses (Δv_1 and Δv_2) keep the direction of the orbits' motion.

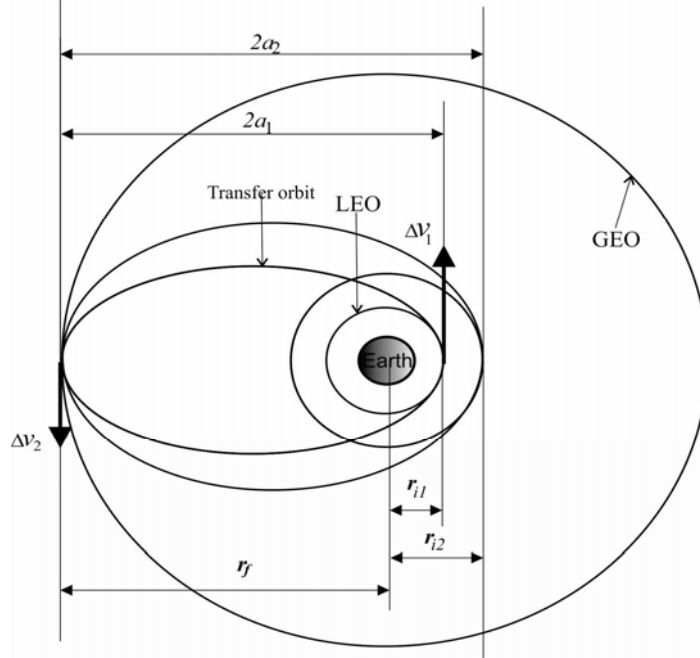


FIGURE 2. HOHMANN COPLANAR TRANSFER ORBIT.

Since our goal is to calculate the thrust (impulse) velocities to be applied at LEO orbits of different radii, than $r_{i1}, r_{i2}, \dots, r_{in}$ denote the radii of initial low Earth circular orbits. This fact causes different major axis of transfer orbits as $2a_1, 2a_2, \dots, 2a_n$. Under these considerations r_f remains unchangeable and it is the radius of geosynchronous orbit as $r_f = 42164\text{km}$.

$$2a_n = r_f + r_{in} \quad (15)$$

Based on (10) will have the velocity of initial circular orbit as v_{in} and the velocity of final circular orbit as v_f . Thus, v_{in} depends on the LEO radius r_{in} , and v_f remains unchangeable because of r_f unchangeability.

$$v_{in} = \sqrt{\frac{\mu}{r_{in}}} \quad (16)$$

$$v_f = \sqrt{\frac{\mu}{r_f}} \quad (17)$$

For elliptic orbit with perigee equal to r_{in} and apogee of r_f the velocities at perigee and apogee are:

$$v_{pn} = \sqrt{\left(\frac{2\mu}{r_{in}}\right) - \left(\frac{2\mu}{r_{in} + r_f}\right)} \quad (18)$$

$$v_{an} = \sqrt{\left(\frac{2\mu}{r_f}\right) - \left(\frac{2\mu}{r_{in} + r_f}\right)} \quad (19)$$

v_{pn} is in fact the velocity in the transfer orbit at initial orbit height and v_{an} in fact is the velocity in the transfer orbit at final orbit height. The initial velocity increment (Δv_{in}), to move the satellite from the initial circular orbit to the elliptic transfer orbit, is given as the difference between velocity at perigee of transfer orbit v_{pn} and the velocity of

the initial circular orbit v_{in} and the as:

$$\Delta v_{1n} = v_{pn} - v_{in} \quad (20)$$

The final velocity increment (Δv_{2n}), to move the satellite from elliptic transfer orbit to geosynchronous circular orbit, is given as the difference between the velocity on the final circular v_f orbit and the velocity on the apogee of the transfer elliptical orbit v_{an} .

$$\Delta v_{2n} = v_f - v_{an} \quad (21)$$

Applying (18) to (21) will have,

$$\Delta v_{1n} = \sqrt{\frac{\mu}{r_{in}}} \left(\sqrt{\frac{2r_f}{r_{in} + r_f}} - 1 \right) \quad (22)$$

$$\Delta v_{2n} = \sqrt{\frac{\mu}{r_f}} \left(1 - \sqrt{\frac{2r_f}{r_{in} + r_f}} \right) \quad (23)$$

Further it is defined normalized radius R_n as follows,

$$R_n = \sqrt{\frac{r_{in}}{r_f}} \quad (24)$$

from which one yields out

$$v_f = R_n \cdot v_{in} \quad (25)$$

Applying (24) and (25) at (22) and (23), finally will have velocity increments to be applied at Hohmann coplanar transfer orbit in order to attain geosynchronous orbit from different low Earth orbits, as:

$$\Delta v_{1n} = v_{in} \cdot \left(\sqrt{\frac{2}{R_n^2 + 1}} - 1 \right) \quad (26)$$

$$\Delta v_{2n} = v_{in} \cdot R_n \cdot \left(1 - R_n \cdot \sqrt{\frac{2}{R_n^2 + 1}} \right) \quad (27)$$

From the propellant consumption point of view, it of interest the contribution of both velocity impulses as:

$$\Delta v_n = \Delta v_{1n} + \Delta v_{2n} \quad (28)$$

The eccentricity of the transfer orbit for different low Earth orbits is given as,

$$e_n = \frac{1 - R_n^2}{1 + R_n^2} \quad (29)$$

Calculations and Results

The transfer is initiated by firing the space craft engine at low Earth orbit in order to accelerate it so that it will follow the elliptical orbit; this adds energy to the space craft's orbit. When the spacecraft has reached transfer orbit, its orbital speed (and hence its orbital energy) must be increased again in order to change the elliptic orbit to the larger circular one, respectively to geosynchronous one.

For simulation purposes five altitudes of low Earth orbits are considered as initial orbits for the Hohmann transfer, starting from altitude of 500km up to 1300km which are typical for LEO satellites. These altitudes correspond to initial radii of 6878km up to 7678km. For each of them it is calculated (Δv_1) and (Δv_2) additionally (Δv). These results are presented in Table 1 and in Figure 3.

TABLE 1. VELOCITY IMPULSES TO BE APPLIED AT ELLIPTIC HOHMANN TRANSFER ORBIT.

n	1	2	3	4	5
h_n (km)	500	700	900	1100	1300
r_{in} (km)	6878	7078	7278	7478	7678
v_{in} (km/s)	7.587	7.479	7.376	7.277	7.181
R_{in}	0.403	0.409	0.415	0.421	0.426
e_n	0.721	0.713	0.706	0.699	0.692
Δv_{1n} (km/s)	2.359	2.311	2.257	2.204	2.161
Δv_{2n} (km/s)	1.443	1.422	1.405	1.384	1.364
Δv_n (km/s)	3.802	3.733	3.662	3.588	3.525

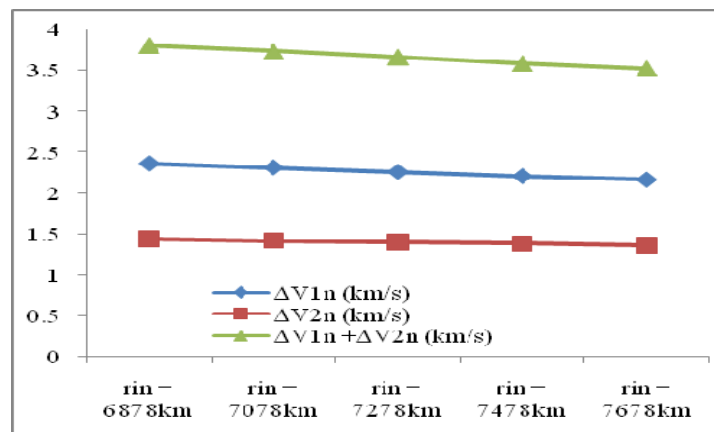


FIGURE 3. VELOCITY VARIATIONS UNDER DIFFERENT INITIAL ORBIT ALTITUDES.

Figure 3, confirms that as higher is the altitude of the low initial orbit, the lower velocity impulse is needed to the final destination orbit. Consequently less fuel is needed to be carried out on the satellite in case that the satellite initially is injected on the higher altitude toward the final geosynchronous destination.

Conclusions

In orbital mechanics, the Hohmann transfer orbit is an elliptical orbit used to transfer between two circular orbits of different radii. If both orbits lie in the same plane, it is known as coplanar transfer. The orbital maneuver to perform the Hohmann transfer applies two engine impulses (thrusts), one to move a space craft onto the transfer orbit and a second to move off it.

It is confirmed that as higher is the altitude of the low initial orbit, the lower velocity impulse is needed to the final destination orbit. Consequently less fuel is needed to be carried out on the space craft in case that the space craft initially is injected on the higher altitude.

Through simulation results, it is also confirmed that for different altitudes of initial orbit, the first velocity impulse has faster decreasing gradient than the second velocity impulse.

REFERENCES

- [1] P. V. Arluklar, S.D. Naik, "Optimality of generalized Hohmann transfer using dynamical approach Lambert solution", *International Journal of Applied Mathematics and Mechanics*, 8 (10), 28-37, 2012.
- [2] O. M. Kamel, Adel S. Soliman, "The generalized Hohmann transfer with plane change using energy concepts", Part I, *Mechanics and Mechanical Engineering*, 15 (2), 183-191, 2011.
- [3] The Hohmann Orbit Transfer - Orbital And Celestial Mechanics, <http://www.cdeagle.com/omnum/pdf/hohmann.pdf>
- [4] D. Roddy, "Satellite communications", McGraw Hill, New York, 2006.

- [5] M. Richharia, (1999), "Satellite communication systems", McGraw Hill, New York, 1999.
- [6] S. Cakaj, "Horizon Plane and Communication Duration for Low Earth Orbiting (LEO) Satellite Ground Stations", WSEAS Journal: Transactions on Communications, Issue 4, Volume 8, April 2009, pp. 373-383.
- [7] S. Cakaj, "Rain Attenuation Impact on Performance of Satellite Ground Stations for LowEarth Orbiting (LEO) Satellites in Europe", International Journal of Communications, Networks and System Sciences (IJCNS), Volume 2, Number 6, September 2009, USA, pp. 480-485.
- [8] S. Cakaj, K. Malaric, A. L. Scholtz, "Modelling of Interference Caused by Uplink Signal for Low Earth Orbiting Satellite Ground Stations", 17th IASTED International Conference on Applied Simulation and Modelling, ASM 2008, June, 23 -25, 2008, Corfu, Greece, pp. 187-191.
- [9] Z. Ismail and R. Varatharajoo," A study of reaction wheel configuration for a 3-axis satellite attitude control", Journal: Advances in Space Research, Issue 6, Volume 45, 2009, pp. 750-759.
- [10]R. Esmailzadeh, H. Arefkhani, S. Davoodi, "Active control and attitude stabilization of a momentum-biased satellite without yaw measurements", Proceedings: 19th Iranian Conference on Electrical Engineering (ICEE), 2011, May 2011, pp. 1-6.
- [11]M. Reyhanoglu, S. Drakunov,"Attitude stabilization of small satellites using only magnetic actuation", 34th Conference on Industrial Electronics (IECON), 2008,pp. 103-107.
- [12]H. Min, at al. "Optimal collision avoidance maneuver control for formation flying satellites using linear programming", Proceedings: 29th Chinese Control Conference (CCC), 2010, pp. 3390-3393.
- [13]A. Mohammadi, at al. "On application of Q-guidance method for satellite launch systems", 3rd International Symposium on Systems and Control in Aeronautics and Astronautics (ISSCAA), 2010, pp.1314-1319.
- [14]J. Pearson, "Low cost launch systems and orbital fuel depot", Acta Astronautica, Vol 18(4), pp. 315-320, 1999.



Shkelzen Cakaj has received his BSc and MSc degrees from Prishtina University in Kosovo. Since 2003 is cooperating with Institute for Communication and Radio – Frequency Engineering at the Technical University in Vienna, where he has prepared his Master Thesis related to the performance of the ground satellite station in July, 2004. He was awarded a PhD in area of satellite communication from Zagreb University in January 2008 with whom he has continued technical associations. He has attended courses on satellite communication and spectrum management at USTTI. He was awarded as Fulbright scholar researcher in 2009 at NOAA (National Oceanic and Atmospheric Administration) at Maryland, USA. He is the author of 50 papers published in worldwide conferences and journals; mostly IEEE. His area of interest is the performance of satellite ground stations for scientific satellites. He is working at Post and Telecommunication of Kosovo and lecturing satellite communications for master students at Prishtina University, Kosovo and Polytechnic University of Tirana, Albania.